

REAL-TIME DESCRIPTION OF PARTON-HADRON CONVERSION AND CONFINEMENT DYNAMICS

John Ellis and Klaus Geiger

CERN TH-Division, CH-1211 Geneva 23, Switzerland

Abstract

We propose a new and universal approach to the hadronization problem that incorporates both partonic and hadronic degrees of freedom in their respective domains of relevance, and that describes the conversion between them within a kinetic field theory formulation in real time and full 7-dimensional phase space. We construct a scale-dependent effective theory that reduces to perturbative QCD with its scale and chiral symmetry properties at short space-time distances, but at large distances ($r \gtrsim 1$ fm) yields symmetry breaking gluon and quark condensates plus hadronic excitations. The approach is applied to the evolution of fragmenting $q\bar{q}$ and gg jet pairs as the system evolves from the initial 2-jet configuration, via parton showering and cluster formation, to the final yield of hadrons. The phenomenological implications for $e^+e^- \rightarrow \text{hadrons}$ are investigated, such as the time scale of the transition, and its energy dependence, cluster size and mass distributions. We compare our results for particle production and Bose-Einstein correlations with experimental data, and find an interesting possibility of extracting the basic parameters of the space-time evolution of the system from Bose enhancement measurements.

johne@cernvm.cern.ch

klaus@surya11.cern.ch

1. INTRODUCTION

The physics of QCD exhibits different relevant excitations at distinct length (or momentum) scales. To give this notion a well-defined meaning, consider some characteristic length scale L_c of the order of 1 fm that crudely separates short- from long-distance physics. At short space-time distances ($r \ll L_c$) the relevant degrees of freedom are quarks and gluons, effectively unconfined due to asymptotic freedom, and their interactions are well described by perturbative QCD. The theory exhibits chiral symmetry and (approximate) scale symmetry. At large distances ($r \gg L_c$) on the other hand, we are in the regime of hadronic degrees of freedom and physical observable particles, whose non-perturbative interactions are known to be described well by chiral models. In between these two regimes, in the range $r \approx L_c$, our current knowledge is essentially limited to the understanding that there must be a rather sudden dynamical establishment of long-range order, i.e. some kind of “phase transition” from the unconfined, chiral- and scale-invariant phase of partons to the hadronic phase with massive physical states and broken symmetries.

The *dynamics* of this parton-hadron conversion and confinement mechanism has scarcely been studied yet, although QCD-inspired effective quark models that incorporate confinement phenomenology in some way have been exploited extensively to describe static hadron properties rather well [1]. This problem is particularly serious for attempts to describe the phenomenon of hadronization in high-energy QCD processes. The theoretical tools currently available for studying QCD are inadequate to describe the transformation from partonic to hadronic degrees of freedom as a dynamic process: perturbative techniques [2] are limited to the short-distance regime where confinement is not apparent, whilst effective low-energy chiral models [3] and QCD sum rules [4], that incorporate confinement, lack partonic degrees of freedom. On the other hand, common descriptions of parton fragmentation [5] are usually based on ad hoc prescriptions to simulate hadron formation from parton decays. In principle, lattice QCD [6] should be able to bridge the gap, but in practice dynamical calculations of parton-hadron conversion are not yet feasible.

The purpose of the present paper is to give a detailed documentation of our progress towards a consistent, fully dynamical formulation of the non-static properties of confinement, chiral symmetry breaking and hadron formation, as recently proposed in Ref. [7]. Aside from the aforementioned arguments, these issues are of great interest in the context

of the QCD phase transition in the early Universe when hadrons formed from unconfined quark-gluon matter, or in high-energy heavy-ion collisions, where one expects a very hot and dense deconfined quark-gluon plasma to be created. Here it is inevitable to employ a dynamical treatment of the transition from short-distance (perturbative) regime of partons to the long-distance (non-perturbative) domain of hadrons. We extend here previous work [8] and present a universal approach to the dynamic transition *between* partons and hadrons based on an effective QCD field theory description and relativistic kinetic theory.

Our concept is the following: we start from a gauge-invariant Lagrangian formulation that embodies both fundamental partonic and composite hadronic degrees of freedom. It is explicitly dependent on the space-time scale $L = \sqrt{r^2}$ at which the physics is “probed”. The scale dependence is however not external, but the variation of the scale is governed by the dynamical evolution of the physical system under consideration. The field equations of motion can be cast into evolution equations for the real-time Green functions of the various particle species, and by following the space-time evolution we can trace the conversion from partonic to hadronic degrees of freedom in full 7-dimensional phase space, as it is driven by the dynamics. This effective field theory approach recovers QCD with its scale and chiral symmetry properties at short distances or high momentum transfers, but yields at low energies the formation of symmetry breaking gluon and quark condensates including excitations that represent the physical hadrons.

It is important to explain in more detail the physical basis of our approach: we assume that the vacuum state in QCD can be visualized as a “color dielectric medium” [9] characterized by some collective color-singlet fields that correspond in the long-wavelength limit to the gluon and quark condensates, and incorporate phenomenologically the complex structure of the physical vacuum as order parameters. Specifically, the underlying hypothesis [10, 11] is that the *long-distance* (non-perturbative) gluon self-interactions generate an effective *scalar gluon condensate field* χ which is self-interacting through some potential V constructed [14] on the basis of the symmetry properties of the QCD Lagrangian. As a consequence of symmetry constraints, the scalar field χ must in addition couple through the potential V to an effective *pseudoscalar quark condensate field* U , a feature which is also suggested by lattice QCD studies [6], indicating that the confining and chiral symmetry breaking “phase transitions” are in some way related and occur approximately at the

same scale. The long-range properties of the non-perturbative vacuum are then characterized by gluon and quark condensates which are proportional to the non-vanishing vacuum expectation values $\langle\chi\rangle \equiv \chi_0$ and $\langle U\rangle \equiv U_0$ in the long-distance limit.

Our central idea is that the effective gluon condensate field χ plays the driving role in the generation of confinement and chiral-symmetry-breaking mechanisms: the non-perturbative gluon self-interactions are assumed to modify the long-range properties of the vacuum in such a way that the propagation of the *elementary gluon fields* A^μ is altered with increasing space-time distances and eventually completely suppressed (confinement). As a direct consequence [11], the self-energy of the *elementary quark fields* ψ will be modified accordingly through the quark-gluon coupling, so that it generates dynamically an effective quark mass term which becomes infinite at large space-time distances. The coupling between the perturbative regime with elementary fields A^μ , ψ and the non-perturbative vacuum represented by the condensate fields χ , U is mediated by a single dimensionless “color-dielectric function” $\kappa(\chi)$ [15], which vanishes in the short-distance limit, but approaches unity at large distances. There is no need to introduce an additional coupling to the field U , nor to consider an explicit chiral-symmetry-breaking quark mass term, because, as mentioned, the quarks acquire a dynamic mass via their coupling to the gluons in the presence of the field χ .

We thus obtain an effective QCD field theory which in the short distance limit ($\langle\chi\rangle = 0, \langle U\rangle = 0, \kappa(0) = 1$) is chiral invariant and incorporates free gluon and quark propagation (asymptotic freedom), whereas in the long distance limit ($\langle\chi\rangle = \chi_0, \langle U\rangle = U_0, \kappa(\chi_0) = 0$) no gluon or quark propagation can occur (confinement). In between these two regimes, the effective theory interpolates and governs the dynamics of the conversion of short-distance fluctuations (partons) to non-perturbative bound states (hadrons) embedded in the physical vacuum. As a prototype case, we study in detail the parton-hadron conversion in $e^+e^- \rightarrow \text{hadrons}$. We visualize the process $e^+e^- \rightarrow \bar{q}q$ as producing a “hot spot” in which the long-range order represented by χ_0 and U_0 is disrupted locally by the appearance of a bubble of the naive perturbative vacuum. Within this bubble, a parton shower develops in the usual perturbative way, with the hot spot expanding and cooling in an irregular stochastic manner described by QCD transport equations. This perturbative description remains appropriate in any phase-space region of the shower where the local energy density is large

compared with the difference in energy density between the perturbative partonic and the non-perturbative hadronic vacua. When this condition is no longer satisfied, a bubble of hadronic vacuum may be formed with a probability determined by statistical-mechanical considerations.

This paper is organized in two main parts. The first part, consisting of Secs. 2 and 3, is intended as a comprehensive presentation of the general field-theoretical framework and necessary elements of quantum transport theory. In Sec. 2 we construct on the basis of the dual vacuum picture of coexisting perturbative and non-perturbative domains an effective theory that embodies the correct scale and symmetry properties of QCD and that has the desired features outlined above. We also discuss the relation to the phenomenology of the QCD phase transition, where the role of the critical temperature is analogous to the critical confinement length scale in our approach. Sec. 3 outlines the method of real-time Green functions that we use to derive from the field equations of motion the corresponding coupled equations for the particle distribution functions. We also indicate how macroscopic quantities related to observables can be extracted from the microscopic particle dynamics within the kinetic theory of (non-equilibrium) many-particle systems. The second part of the paper, Secs. 4-6, is devoted to the application of this effective QCD field theory to the dynamics of parton-hadron conversion for the prototype process of fragmenting jet systems initiated by e^+e^- annihilation. In Sec. 4 we derive transport equations that, in the case of the partons, are generalized QCD evolution equations in full phase space, and similar equations for the excitations of the χ and U fields. In Sec. 5 we present results of simulating this real-time evolution of partons through the perturbative shower stage, via subsequent formation of color-singlet clusters, and finally hadronic cluster decay to give the final hadron yield. We investigate phenomenological implications for particle production and the Bose-Einstein effect, which we find to be a particularly sensitive probe to measure and test the confinement dynamics. Finally, Sec. 6 is reserved for a summary and a brief discussion of future perspectives of the approach, in particular its applicability to the QCD phase transition, and to high-density QCD.

2. FIELD THEORY FRAMEWORK

As explained in the introduction, the vacuum state in QCD may be pictured as a color-dielectric medium characterized by long-range order parameters. Consider the vacuum expectation values (*vev*'s) of the normal-ordered products of color-singlet and Lorentz scalar (pseudoscalar) functions $\chi(U)$ [8, 15]

$$\langle 0 | \chi(F_a^{\mu\nu}) | 0 \rangle \quad ; \quad \langle 0 | U(\psi_i, \bar{\psi}_j) | 0 \rangle , \quad (1)$$

where $F_a^{\mu\nu}$ is the usual $SU(3)$ field strength tensor, $\psi, \bar{\psi}$ the quark fields, and $\chi(0), U(0)$ is set to be zero. For instance, χ can be $f_{abc}F_{\mu\nu}^a F_{\nu\lambda}^b F_{\lambda\mu}^c$ or $(F_{\mu\nu}^a F_{\mu\nu}^a)^2$, or other combinations. Similarly, U may be composed of $Tr[(\bar{\psi}_i \psi_j)^2]$, $Tr[(\bar{\psi}_i \bar{\psi}_j \psi_k \psi_l)^2]$, etc.. These *vev*'s are physical quantities that characterize the structure of the QCD vacuum [16] and are related to the measurable gluon and quark condensates, respectively.

Clearly, if we take the long wavelength limit $L \rightarrow \infty$ and simultaneously let the coupling strength g_s among the fields tend to zero, we have in general the non-comutativity of the double limits

$$\begin{aligned} \lim_{L \rightarrow \infty} \lim_{g_s \rightarrow 0} \langle 0 | \chi(F_a^{\mu\nu}) | 0 \rangle &= 0 \quad \neq \quad \lim_{g_s \rightarrow 0} \lim_{L \rightarrow \infty} \langle 0 | \chi(F_a^{\mu\nu}) | 0 \rangle \\ \lim_{L \rightarrow \infty} \lim_{g_s \rightarrow 0} \langle 0 | U(\psi_i, \bar{\psi}_j) | 0 \rangle &= 0 \quad \neq \quad \lim_{g_s \rightarrow 0} \lim_{L \rightarrow \infty} \langle 0 | U(\psi_i, \bar{\psi}_j) | 0 \rangle , \end{aligned} \quad (2)$$

with $\langle 0 | F_a^{\mu\nu} | 0 \rangle = 0 = \langle 0 | \psi_i | 0 \rangle$. Eq. (2) is a pure quantum phenomenon and a typical property of phase transitions. It implies that there is long-range order in the vacuum which can be characterized by the operator functions χ and U .

In order to embody this concept into a field theory formulation, let us define the *distance measure* L for the space-time separation between two points r and r' ($r^\mu = (t, \vec{r})$):

$$L := \sqrt{(r - r')_\mu (r - r')^\mu} , \quad (3)$$

and introduce a *characteristic length scale* L_c that separates short distance ($L \ll L_c$) and long range ($L \gtrsim L_c$) physics in QCD. The scale L_c can be associated with the confinement length of the order of a hadron radius, as we will specify more precisely later.

2.1 The short-distance regime $L \ll L_c$

At *small space-time distances* $L \ll L_c$, because of asymptotic freedom, the properties of QCD are well described by a perturbative expansion in powers of the coupling g_s of the generating functional for the connected Green functions,

$$W[J, \eta, \bar{\eta}] = \int \mathcal{D}A^\mu \mathcal{D}\psi \mathcal{D}\bar{\psi} \det \mathcal{F} \exp \left\{ i \int d^4r \left(\mathcal{L}[A^\mu, \psi, \bar{\psi}] + J_{\mu,a} A_a^\mu + \bar{\psi}_i \eta + \bar{\eta} \psi_i \right) \right\}. \quad (4)$$

In the path integral, $\det \mathcal{F}$ denotes the Fadeev-Popov determinant and J , η , $\bar{\eta}$ are the generating currents for the gluon fields A_a^μ and the quark fields ψ , $\bar{\psi}$ (which are vectors in flavor space, $\psi \equiv (\psi_u, \psi_d, \dots)$), and the QCD Lagrangian is

$$\mathcal{L}[A^\mu, \psi, \bar{\psi}] = -\frac{1}{4} F_{\mu\nu,a} F_a^{\mu\nu} + \bar{\psi}_i \left[(i\gamma_\mu \partial^\mu - m) \delta_{ij} - g_s \gamma_\mu A_a^\mu T_a^{ij} \right] \psi_j + \xi_a(A), \quad (5)$$

where $F_a^{\mu\nu} = \partial^\mu A_a^\nu - \partial^\nu A_a^\mu + g_s f_{abc} A_b^\mu A_c^\nu$ is the gluon field-strength tensor. The subscripts a, b, c label the color components of the gluon fields, and g_s denotes the color charge related to $\alpha_s = g_s^2/(4\pi)$. The T_a are the generators of the $SU(3)$ color group, satisfying $[T_a, T_b] = if_{abc} T_c$ with the structure constants f_{abc} . The indices i, j label the color components of the quark fields and $m \equiv \text{diag}(m_u, m_d, \dots)$. Throughout, summation over the color indices a, b, c and i, j is understood. We recall that on setting the quark current masses m to zero, one has exact chiral symmetry. The gauge-fixing term is denoted by a general function $\xi_a(A)$ which, e.g., in covariant gauges is $\xi_a(A) \equiv -1/(2\alpha)(\partial_\mu A_a^\mu)^2$ with Lagrange multiplier $1/\alpha$. However, we will later consider a different (ghost-free) gauge that is more convenient for our purposes.

2.2 The long-distance regime $L \gg L_c$

The long-range physics of QCD at *large space-time distances* $L \gg L_c$, is known to be described well by an effective low-energy theory. Here we adopt the approach of Ref. [14] and define the corresponding generating functional as:

$$W[J_\chi, K_U, K_U^\dagger] = \int \mathcal{D}\chi \mathcal{D}U \mathcal{D}U^\dagger \exp \left\{ i \int d^4r \left(\mathcal{L}[\chi, U, U^\dagger] + J_\chi \chi + U^\dagger K_U + K_U^\dagger U \right) \right\}. \quad (6)$$

The field degrees of freedom are a *scalar gluon condensate field* χ and a *pseudoscalar quark condensate field* $U = f_\pi \exp \left(i \sum_{j=0}^8 \lambda_j \phi_j / f_\pi \right)$ for the nonet of the meson fields ϕ_j ($f_\pi = 93$

MeV, $Tr[\lambda_i \lambda_j] = 2\delta_{ij}$, $UU^\dagger = f_\pi^2$, with non-vanishing vev 's in the long-distance limit,

$$\chi_0 := \frac{\delta}{\delta J_\chi} \ln W[J_\chi, K_U, K_U^\dagger] = \frac{\langle 0 | \chi | 0 \rangle}{\langle 0 | 0 \rangle} \neq 0 \quad (7)$$

$$U_0 := \left(\frac{\delta}{\delta K_U^\dagger} + \frac{\delta}{\delta K_U} \right) \ln W[J_\chi, K_U, K_U^\dagger] = \frac{\langle 0 | U + U^\dagger | 0 \rangle}{\langle 0 | 0 \rangle} \neq 0, \quad (8)$$

and an effective action

$$\begin{aligned} \Gamma[\chi, U, U^\dagger] &\equiv \ln W[J_\chi, K_U, K_U^\dagger] - \int d^4r \left\{ J_\chi \chi + U^\dagger K_U + K_U^\dagger U \right\} \\ &= \int d^4r \left\{ -V(\chi, U) + \frac{1}{2} (\partial_\mu \chi)(\partial^\mu \chi) + \frac{1}{4} Tr \left[(\partial_\mu U)(\partial^\mu U^\dagger) \right] + \dots \right\}. \end{aligned} \quad (9)$$

Consequently the Lagrangian in (6) is given by

$$\mathcal{L}[\chi, U, U^\dagger] = \frac{1}{2} (\partial_\mu \chi)(\partial^\mu \chi) + \frac{1}{4} Tr \left[(\partial_\mu U)(\partial^\mu U^\dagger) \right] - V(\chi, U), \quad (10)$$

with a potential V that has been constructed [12, 13] on the basis of constraints which arise from the scale and chiral symmetry properties of the exact QCD Lagrangian, namely,

$$\begin{aligned} V(\chi, U) &= b \left[\frac{1}{4} \chi_0^4 + \chi^4 \ln \left(\frac{\chi}{e^{1/4} \chi_0} \right) \right] + \frac{1}{4} \left[1 - \left(\frac{\chi}{\chi_0} \right)^2 \right] Tr \left[(\partial_\mu U)(\partial^\mu U^\dagger) \right] \\ &\quad + c Tr \left[\hat{m}_q (U + U^\dagger) \right] \left(\frac{\chi}{\chi_0} \right)^3 + \frac{1}{2} m_0^2 \phi_0^2 \left(\frac{\chi}{\chi_0} \right)^4. \end{aligned} \quad (11)$$

Here the parameter b is related to the conventional bag constant B by

$$B = b \frac{\chi_0^4}{4}. \quad (12)$$

Furthermore, c is a constant of mass dimension 3, $m_q = \text{diag}(m_u, m_d, m_s)$ is the light quark mass matrix, and m_0^2 is an extra U(1)-breaking mass term for the ninth pseudoscalar meson ϕ_0 (which we will disregard in the following). In the chiral limit, this potential has a minimum when $\langle \chi \rangle = \chi_0$ and equals the vacuum pressure B at $\langle \chi \rangle = 0$.

2.3 The intermediate regime $L \approx L_c$

Having established a field theory framework for the two regions $L \ll L_c$ and $L \gg L_c$, the crucial issue is now the intermediate range. Clearly there must be a dynamical interpolation around $L \approx L_c$ from the short-range to the long-range description. We propose here the following approach. Let us first consider the long-range domain, i.e. the physical vacuum characterized by χ_0 , and introduce into the vacuum an excitation of small space-time extent.

For instance, imagine the creation of a $q\bar{q}$ pair with invariant mass $Q \simeq L^{-1} \gg L_c^{-1}$ by a time-like virtual photon from e^+e^- annihilation. The insertion of such a localized excitation (“hot spot”) modifies the vacuum and we assume that the corresponding change in the action integral $S \equiv \int d^4r \mathcal{L}[\chi, U, U^\dagger]$ in (6) can be evaluated sufficiently accurately to second order as

$$\begin{aligned} \delta S &= \frac{1}{2} \int d^4r \left\{ \left\langle 0 \left| \frac{\delta^2 \mathcal{L}[\chi, U, U^\dagger]}{\delta F_{\mu\nu,a} \delta F_b^{\mu\nu}} \right| 0 \right\rangle F_{\mu\nu,a} F_b^{\mu\nu} \delta_{ab} + \left\langle 0 \left| \frac{\delta^2 \mathcal{L}[\chi, U, U^\dagger]}{\delta \psi_i \delta \bar{\psi}_j} \right| 0 \right\rangle \psi_i \bar{\psi}_j \delta_{ij} \right\} \\ &= \int d^4r \left\{ -\frac{\kappa_L(\chi)}{4} F_{\mu\nu,a} F_a^{\mu\nu} - \mu_L(\chi) \bar{\psi}_i \psi_i \right\}, \end{aligned} \quad (13)$$

where κ_L and μ_L refer to the appropriate vev ’s. Note that this change δS in the action preserves local gauge invariance. We also remark that this ansatz implicitly assumes that the elementary gluon ($F_{\mu\nu}$) and quark fields ($\psi, \bar{\psi}$) couple directly only to the scalar field χ , but not to the pseudoscalar field U . The dynamics of U is solely driven by its coupling to χ through the potential $V(\chi, U)$, eq. (11).

On the other hand, we know that the short-range properties at $L \ll L_c$ of our $q\bar{q}$ excitation are not affected by the long-range correlations. Thus, here we can use (5) with perturbative methods, since the quanta are asymptotically free and $\langle \chi \rangle = 0 = \langle U + U^\dagger \rangle$. Thus we can combine (5) and the effect of (13) by adding to $\mathcal{L}[A^\mu, \psi, \bar{\psi}]$ and $\mathcal{L}[\chi, U, U^\dagger]$ the following contribution that carries an explicit scale- (L -)dependence:

$$\mathcal{L}_L[A^\mu, \psi, \bar{\psi}, \chi] = \int d^4r \left\{ \frac{1}{4} \left(1 - \kappa_L(\chi) \right) F_{\mu\nu,a} F_a^{\mu\nu} - \mu_L(\chi) \bar{\psi}_i \psi_i - \left(1 - \kappa_L(\chi) \right) \xi_a(A) \right\}, \quad (14)$$

where the third term in the integrand is necessary to maintain local gauge invariance. It remains to specify the form of the functions $\kappa_L(\chi)$ and $\mu_L(\chi)$. Since κ_L has to satisfy the boundary conditions [15]

$$\kappa_L(0) = 1, \quad \kappa_L(\chi_0) = 0, \quad (15)$$

and is constrained to be a Lorentz-invariant color-singlet function of scale dimension zero, a minimal possibility is

$$\kappa_L(\chi) = 1 - \left(\frac{L\chi}{L_0\chi_0} \right)^2. \quad (16)$$

It turns out that the particular form of $\kappa_L(\chi)$ is not crucial as long as the properties (15) are satisfied [17], because parton-hadron conversion is quite rapid, as we see later, being related

to the weakly first-order nature of the QCD phase transition at finite temperature. The essence is that (16) enforces color charge confinement due to the fact that a color electric charge creates a displacement $\vec{D}_a = \kappa_L \vec{E}_a$, where $E_a^k = F_a^{0k}$, with energy $\frac{1}{2} \int d^3r D_a^2 / \kappa_L$ which becomes infinite at large r for non-zero total charge.

Similarly, absolute confinement can be ensured also for quarks by coupling the quark fields to the χ field through

$$\mu_L(\chi) = \mu_0 \left(\frac{1}{\kappa_L(\chi)} - 1 \right) = \frac{\mu_0 (L\chi)^2}{(L_0\chi_0)^2 - (L\chi)^2}, \quad (17)$$

where μ_0 is a constant of mass dimension one that we will set equal to 1 GeV. This form reflects that the quark mass term $\mu_L(\chi)$ in (14) is induced by non-perturbative gluon interactions, rather than being an independent quantity, as is suggested by an explicit calculation [11] of the quark self-energy involving the gluon propagator in the presence of the collective field χ . It has been shown [10] that the dynamical mass $\mu_L(\chi)$ leads to an effective confinement potential with the masses of the quarks at small L approximately equal to the current masses, but at large L when $\langle \chi \rangle \rightarrow \chi_0$ it generates an infinite asymptotic quark mass,

$$\mu_L(0) = 0, \quad \mu_L(\chi_0) = \infty. \quad (18)$$

It is evident from (16)-(18) that $\mathcal{L}[A^\mu, \psi, \bar{\psi}, \chi]$ given by (14) vanishes in the short-distance limit ($L \rightarrow 0, \langle \chi \rangle \rightarrow 0$), whereas in the long-distance limit it suppresses the propagation of colored gluon and quark fluctuations, and interpolates smoothly between the two extremes. The typical functional forms of $\kappa_L(\chi)$ and $\mu_L(\chi)$ are illustrated in Fig. 1.

2.4 The scale-dependent generating functional for the effective theory

Let us now summarize and combine the three contributions of Secs. 2.1-2.3 into a single action integral, and write down the resulting generating functional as an effective description covering the full range $0 < L < \infty$ and depending implicitly on the scale L as defined by (3):

$$\begin{aligned} W_L[J, \eta, \bar{\eta}, J_\chi, K_U, K_U^\dagger] &= \int \mathcal{D}A^\mu \mathcal{D}\psi \mathcal{D}\bar{\psi} \mathcal{D}\chi \mathcal{D}U \mathcal{D}U^\dagger \det \mathcal{F} \\ &\times \exp \left\{ i \int d^4r \left(\mathcal{L}[A^\mu, \psi, \bar{\psi}] + \mathcal{L}_L[A^\mu, \psi, \bar{\psi}, \chi] + \mathcal{L}[\chi, U, U^\dagger] \right. \right. \\ &\quad \left. \left. + J_{\mu,a} A_a^\mu + \bar{\psi} \eta + \bar{\eta} \psi J_\chi \chi + U^\dagger K_U + K_U^\dagger U \right) \right\}, \end{aligned} \quad (19)$$

where $\mathcal{L}[A^\mu, \psi, \bar{\psi}]$ is given by (5), $\mathcal{L}[\chi, U, U^\dagger]$ by (10), and $\mathcal{L}_L[A^\mu, \psi, \bar{\psi}, \chi]$ by (14), so that the effective, L -dependent Lagrangian density $\mathcal{L}_L \equiv \mathcal{L}[A^\mu, \psi, \bar{\psi}] + \mathcal{L}[\chi, U, U^\dagger] + \mathcal{L}_L[A^\mu, \psi, \bar{\psi}, \chi]$ in the generating functional (19) can be written as

$$\begin{aligned} \mathcal{L}_L = & -\frac{\kappa_L(\chi)}{4} F_{\mu\nu,a} F_a^{\mu\nu} + \bar{\psi}_i \left[\left(i\gamma_\mu \partial^\mu - \mu_L(\chi) \right) \delta_{ij} - g_s \gamma_\mu A_a^\mu T_a^{ij} \right] \psi_j + \kappa_L(\chi) \xi_a(A) \\ & + \frac{1}{2} (\partial_\mu \chi)(\partial^\mu \chi) + \frac{1}{4} \text{Tr} \left[(\partial_\mu U)(\partial^\mu U^\dagger) \right] - V(\chi, U), \end{aligned} \quad (20)$$

where $V(\chi, U)$ is the potential given by (11), and we have gone over to the limit of zero current quark masses. It is important to realize that the scale dependence of (19) and (20) arises solely through the L -dependent functions $\kappa_L(\chi)$ and $\mu_L(\chi)$, given by eqs. (16) and (17). The scale L is *not* to be misunderstood as an external parameter. Instead it is intrinsic variable of the formulation. As we will see later, the variation of L is governed by the dynamics of the fields itself, and it in turn determines the time evolution of the interacting fields. Therefore, when studying the dynamical evolution of some system under consideration, one must necessarily require this self-consistency for a meaningful solution.

At this point let us state clearly the following important remarks:

a) The effective field theory defined by (19) and (20) represents a description of the duality of partonic and hadronic degrees of freedom: high-momentum, short-distance quark-gluon fluctuations (the perturbative excitations) are embedded in a collective field χ (the non-perturbative vacuum), in which by definition the low-momentum, long-range fluctuations are absorbed. Confinement is thus associated with a dual structure of the QCD vacuum. The formulation is gauge- and Lorentz-invariant, and is consistent with scale and chiral symmetry properties of QCD. It interpolates between the high-momentum (short-distance) QCD phase with unconfined gluon and quark degrees of freedom and chiral symmetry ($\langle \chi \rangle = 0, \langle U \rangle = 0, \kappa_L = 1, \mu_L = 0$), to a low-energy (long-range) QCD phase with confinement and broken chiral symmetry ($\langle \chi \rangle = \chi_0, \langle U \rangle = U_0, \kappa_L = 0, \mu_L = \infty$), where χ_0 and U_0 are the long-range order parameters of the vacuum, directly related to the gluon condensate and the quark condensate, respectively (Sec. 2.5 below).

b) By introducing additional fields χ and U to describe the long-range behaviour of the gluon and quark fields, we must obviously be careful not to double-count the degrees of freedom, since the full theory of QCD is contained in $\mathcal{L}[A^\mu, \psi, \bar{\psi}]$, eq. (5), already. However, by our construction the sum \mathcal{L}_L in (20) gives a consistent formulation that strictly avoids

double counting, because the introduction of the scale L and the behaviour of the L -dependent coupling functions $\kappa_L(\chi)$ and $\mu_L(\chi)$ truncate the dynamics of the elementary fields A^μ , ψ to the short-distance, high-momentum regime ($L \ll L_c$), whereas the effective description in terms of the collective fields χ , U covers the complementary long-range, low-energy domain ($L \gg L_c$). Accordingly, a quark or gluon is either considered a colored short-range fluctuation (parton) or it is part of a complex bound state (hadron), but not both.

c) The presence of the non-linear coupling function $\kappa_L(\chi)$, which also enters $\mu_L(\chi)$ via (17), means that the sum $\Delta\mathcal{L} \equiv \mathcal{L}[\chi, U] + \mathcal{L}[A^\mu, \psi, \bar{\psi}, \chi]$ in (20) is non-renormalizable. However, there is no need for explicit renormalization, because the composite fields χ and U are already interpreted as effective degrees of freedom with loop corrections implicitly included in $\Delta\mathcal{L}$, and it would be double counting to add them again. Moreover, as mentioned in item b) above, the low-energy domain of $\mathcal{L}[\chi, U]$ is by construction bounded from above by the onset of the high-energy regime described by $\mathcal{L}[A^\mu, \psi, \bar{\psi}]$. The characteristic scale L_c that separates the two domains, therefore, provides an ‘ultra-violet’ cut-off for $\mathcal{L}[\chi, U]$, and at the same time an ‘infra-red’ cut-off for $\mathcal{L}[A^\mu, \psi, \bar{\psi}]$.

2.5 Analogies with QCD at finite temperature

We close this Section with pointing out some immediate phenomenological implications: the particular form (11) of the potential V as a function of χ , as well as the functions κ_L and μ_L that couple short- and long-range regimes, play a central role in dynamical processes where the scale L changes with time. The effect of (14) can be interpreted as a scale- (L -)dependent modification δV , which adds to the (L -independent) potential V , eq. (11),

$$\mathcal{V}(L) := V(\chi, U) + \delta V(L, \chi) , \quad (21)$$

$$\delta V(L, \chi) = \frac{(L\chi)^2}{4(L_0\chi_0)^2} F_{\mu\nu, a} F_a^{\mu\nu} + \frac{\mu_0 (L\chi)^2}{(L_0\chi_0)^2 - (L\chi)^2} \bar{\psi}_i \psi_i . \quad (22)$$

where we used eqs. (16) and (17). We emphasize again that L is not an input parameter, but rather is determined by the space-time dependent separation of the colored quanta. In Sec. 4, we will specify how to determine the variation of the variable L .

In view of (22), one has $\delta V \propto O(L^2)$, therefore it is suggestive that the variable L plays a similar role as the temperature T in finite-temperature QCD, where the correction

to the zero-temperature potential is $O(T^2)$ [18]. This formal analogy will be indicative in the following. However, one must bear in mind that here we are aiming to describe the evolution of a general non-equilibrium system in real time and Minkowski space, as opposed to thermal evolution in Euclidean space. Nevertheless, we adopt the general concept of Ref. [14], and from the analogy with this previous work we can qualitatively expect that the correction δV will give a first-order “phase transition” from the parton to the hadron phase, when combined with V .

As seen in Fig. 2, there are three characteristic scales, L_χ , L_c and L_0 , that mark the time evolution from the small- L to the large- L region as the scale-dependent potential $\mathcal{V}(L)$, eq. (21), changes:

(i) L_χ is the characteristic length scale below which the vacuum with $\chi \neq 0$ cannot exist. The potential \mathcal{V} has a unique minimum at $\chi = 0$, i.e. we are in the perturbative vacuum of the pure parton phase.

(ii) L_c marks the point when the \mathcal{V} develops two degenerate minima, one at $\chi = 0$ and the other at $\chi = \chi_c$. The pressure in the parton phase is here equal to the pressure in the hadron phase, and the probability for partons to tunnel through the barrier becomes large.

(iii) L_0 defines when $\delta V = 0$ and \mathcal{V} becomes equal to V in eq. (11), and has a single absolute minimum at $\langle \chi \rangle = \chi_0$. The parton phase cannot exist any longer, and the parton-hadron conversion is completed. We are in the true (physical) vacuum characterized by the presence of a gluon and a quark condensate.

Following [14], we can relate the vev 's (8), χ_0 and U_0 , to the gluon condensate

$$\langle 0 | \frac{\beta(\alpha_s)}{4\alpha_s} F_{\mu\nu} F^{\mu\nu} | 0 \rangle = -b \chi_0^4 \equiv G_0 \quad (23)$$

and the quark condensate

$$\langle 0 | \bar{q}q | 0 \rangle = c \left(\frac{\chi}{\chi_0} \right)^3 U_0 \equiv Q_0, \quad (24)$$

where b and c are defined in (11). These condensates can be regarded as local order parameters associated with gluon and quark confinement, respectively, and chiral symmetry breakdown. Also, as discussed in [14], one can interpret small oscillations about the minimum of the potential $\mathcal{V} = V$ at $\langle \chi \rangle = \chi_0$, $\langle U + U^\dagger \rangle = U_0$, as physical hadronic states that

emerge after symmetry breaking. They include in principle: (a) glueballs and hybrids as quantum fluctuations in the gluon condensate χ_0 , (b) pseudoscalar mesons as excitations of the quark condensate U_0 , (c) the pseudoscalar flavor singlet meson ϕ_0 , and (d) baryons as topological solitons. We will return below to the issue of hadron formation.

3. EQUATIONS OF MOTION AND KINETIC EVOLUTION

In this Section we outline how to obtain a fully dynamical description of the parton-hadron conversion in real time and complete phase space, starting from the defining generating functional (19) of our effective field theory. A comprehensive derivation can be found in Ref. [19], to which we refer for details. The method is based on the Green function technique [20, 21], here applied to derive transport equations for the field operators A^μ , ψ , χ , and U . The form of the transport equations results directly from the Dyson-Schwinger equations [22]. The self-energy operators that enter the connected part of the equations can then be evaluated in a perturbative expansion. This leads to corresponding equations of motion for the distribution functions of particles, namely gluons and quarks as colored fluctuations, and scalar and pseudoscalar hadronic excitations. The solution for the time development of these particle distribution functions in phase space will then allow us to calculate macroscopic observable quantities within the framework of relativistic kinetic theory.

3.1 Equations of motion

We start from the field equations of motion that follow from the variation of the generating functional (19) with (20):

$$\begin{aligned}
& \left[\left(i\gamma_\mu \partial^\mu - \mu_L(\chi) \right) \delta_{ij} - g_s \gamma_\mu A_a^\mu T_a^{ij} \right] \psi_j = 0 \\
& \partial_\mu F_a^{\mu\nu} + g_s f_{abc} A_{\mu,b} F_c^{\mu\nu} - \left(\partial_\mu \ln \kappa_L(\chi) \right) F_a^{\mu\nu} - \left(1 + \frac{\mu_L(\chi)}{\mu_0} \right) g_s \bar{\psi}_i \gamma^\nu T_a^{ij} \psi_j + \xi_a^\nu(A) = 0 \\
& \partial_\mu \partial^\mu \chi + \frac{\partial V(\chi, U)}{\partial \chi} + \frac{1}{4} \frac{\partial \kappa_L(\chi)}{\partial \chi} F_{\mu\nu,a} F_a^{\mu\nu} + \frac{\partial \mu_L(\chi)}{\partial \chi} \bar{\psi}_i \psi_i = 0 \\
& \partial_\mu \partial^\mu U + \frac{\partial V(\chi, U)}{\partial U} + \partial_\mu \frac{\partial V(\chi, U)}{\partial (\partial_\mu U)} = 0 .
\end{aligned} \tag{25}$$

where $\partial^\mu \equiv \partial/\partial x^\mu$, and we set $U \equiv (U + U^\dagger)/2$. In the second equation, the function

$$\xi_a^\nu(A) := \partial_\mu \left(\kappa_L \frac{\partial \xi_a(A)}{\partial (\partial_\mu A_a^\nu)} \right) \tag{26}$$

results from the gauge-fixing constraint in eq. (5), e.g., in covariant gauges $\xi_a^\nu(A) = (1/\alpha)\partial^\nu\partial_\mu A_a^\mu$. Note that in general there are additional equations of motion involving the ghost fields coupled to the gluon fields, however, since we will later choose a ghost free gauge, these decouple and are irrelevant here.

It is evident from the above equations and the form of the potential $V(\chi, U)$, eq. (11), that in the short-distance limit when $\langle\chi\rangle = 0$ and $\kappa_L(\chi) = 1$, the system of equations decouples and reduces to the usual Yang-Mills equations. Similarly, in the long-wavelength limit, one has $\langle\chi\rangle \rightarrow \chi_0$, $\langle U\rangle \rightarrow U_0$, and $\kappa_L(\chi) \rightarrow 0$, so that the dynamics in this case is completely described by the equations for the effective fields χ and U . A very important point is that the U field does not couple directly to the quark or gluon fields. By construction [14], the dynamics of the quark condensate field U is solely driven by the gluon condensate field χ . As a consequence, the equation for U is readily solved, once the solution for χ is known. It is important to realize that the interplay between the χ field and the quark and gluon fields, ψ and A , is the crucial element of this approach. From a phenomenological point of view, this implies that the transformation of parton to hadron degrees of freedom proceeds first by formation of scalar color-singlet states which subsequently decay into pseudoscalar excitations (Sec. 4).

3.2 Real-time Green functions and microscopic kinetics

The central role in the following is played by the *real-time Green functions* in the ‘closed-time-path formalism’ (for an extensive review, see [21]). This formalism is the appropriate tool to describe general non-equilibrium systems, and its particular strength lies in the possibility of studying the time evolution of phenomena where initial and final states correspond to different vacua, as we are addressing here. In [19] it is shown how one obtains a dynamical formulation which systematically incorporates quantum correlations and describes naturally the transition from the perturbative QCD regime to the non-perturbative QCD vacuum. The real-time Green functions are defined as the two-point functions that measure the *time-ordered correlations* between the fields at space-time points x and y (as before we suppress the spinor indices for the fermion operators):

$$\begin{aligned} i S_{ij}(x, y) &:= \langle T \psi_i(x) \bar{\psi}_j(y) \rangle \\ i D_{ab}^{\mu\nu}(x, y) &:= \langle T A_a^\mu(x) A_b^\nu(y) \rangle \end{aligned}$$

$$\begin{aligned}
i \Delta(x, y) &:= \langle T \chi(x) \chi(y) \rangle - \langle \chi(x) \rangle \langle \chi(y) \rangle , \\
i \tilde{\Delta}(x, y) &:= \langle T U(x) U^\dagger(y) \rangle - \langle U(x) \rangle \langle U^\dagger(y) \rangle ,
\end{aligned} \tag{27}$$

where $\langle \dots \rangle$ denotes the vacuum expectation value, or, in a medium, the appropriate ensemble average, and $T A(x)B(y) = \theta(x_0, y_0)A(x)B(y) \pm \theta(y_0, x_0)B(y)A(x)$ stands for the generalized time-ordering operator along a closed time contour [21] with $+$ ($-$) for boson (fermion) operators. For the χ and U fields, we have subtracted the classical expectation values in order to separate the quantum fluctuations of the fields around the classical field configuration. These Green functions generally describe the propagation of an excitation in a many-particle system from space-time point x to point y . In the absence of a coupling between ψ , A^μ and χ , U , and in the zero-density limit, the expectation values S_{ij} and $D_{ab}^{\mu\nu}$ can be shown [19] to reduce to the usual quark and gluon Feynman propagators, respectively, and Δ with the scalar Feynman propagator.

Using the definitions (27) and implementing the gauge-fixing constraint in (25) for the gluon fields, one finds from (25) the following equations of motion for the Green functions (in the limit of zero rest masses),

$$\begin{aligned}
i\gamma \cdot \partial_x S_{ij}(x, y) &= \delta_{ij} \delta^4(x, y) + \int d^4x' \Sigma_{ik}(x, x') S_{kj}(x', y) \\
\partial_x^2 D_{ab}^{\mu\nu}(x, y) &= \delta_{ab} \delta^4(x, y) \left(g^{\mu\nu} - \mathcal{E}^{\mu\nu} \right) - \int d^4x' \Pi_{\sigma, a, b'}^\mu(x, x') D_{b'b}^{\sigma\nu}(x', y) \\
\partial_x^2 \Delta(x, y) &= -\delta^4(x, y) + \int d^4x' \Xi(x, x') \Delta(x', y) \\
\partial_x^2 \tilde{\Delta}(x, y) &= -\delta^4(x, y) + \int d^4x' \tilde{\Xi}(x, x') \tilde{\Delta}(x', y) ,
\end{aligned} \tag{28}$$

describing the change with respect to x , plus similar equations for the change with y by the substitutions $\partial_x \rightarrow -\partial_y$, and $\Sigma(x, x')S(x', y) \rightarrow S(x, x')\Sigma(x', y)$, etc.. The explicit expressions for the *self energies* Σ , Π , Ξ , and $\tilde{\Xi}$ are rather lengthy and can be found in Ref. [19]. We remark that the functions Σ and Π include both the usual quark and gluon self energies, as well as the additional interaction of the quanta with the χ field. Similarly, the self energy Ξ incorporates the effective self interaction of the χ field described by the potential (11), plus the interaction with the quark and gluon fields in (22). Finally, the self energy of the U field plus its coupling to the χ field is described by $\tilde{\Xi}$. In the equation for the gluon Green

function $D_{ab}^{\mu\nu}$, we have on the right-hand side the remnant of the gauge constraint,

$$\mathcal{E}_{\mu\nu} := \int \frac{d^4 p}{(2\pi)^4} \frac{e^{-i p \cdot (x-y)}}{p^2 + i0^+} \left[g_{\mu\nu} + \sum_{s=1,2} \varepsilon_\mu^\lambda(p, s) \varepsilon_{\lambda\nu}^*(p, s) \right] \quad (29)$$

which involves a sum over the two physical (transverse) gluon polarizations (e.g. in Feynman gauge $\varepsilon_\mu^\lambda = g_\mu^\lambda$ and thus $\sum_s \varepsilon_\mu^\lambda \varepsilon_{\lambda\nu}^* = -g_{\mu\nu}$, i.e. $\mathcal{E}_{\mu\nu} = 0$). We note that equations (28) are of the form of Dyson-Schwinger equations [22], and can be rewritten in symbolic operator notations as

$$\begin{aligned} S &= S_0 + S_0 \Sigma S , & D &= D_0 - D_0 \Pi D \\ \Delta &= \Delta_0 + \Delta_0 \Xi \Delta , & \tilde{\Delta} &= \tilde{\Delta}_0 + \tilde{\Delta}_0 \tilde{\Xi} \tilde{\Delta} , \end{aligned} \quad (30)$$

where S_0 , D_0 , Δ_0 , $\tilde{\Delta}_0$ denote the free-field Green functions that satisfy the equations of motion in the absence of self and mutual interactions. Fig. 3 illustrates the diagrammatic representation of the Green functions $S, D, \Delta, \tilde{\Delta}$, the self-energies $\Sigma, \Pi, \Xi, \tilde{\Xi}$, and the Dyson-Schwinger equations (30).

A quantum transport formalism can be derived from the equations (28) that is very suitable for the present purposes [19]. We confine ourselves here to sketching the essential steps. One introduces the *Wigner transforms* \mathcal{W} [23] of the Green functions and the self energies $W \equiv S, D, \Delta, \Sigma, \Pi, \Xi$:

$$\mathcal{W}(r, p) = \int d^4 R e^{i p \cdot R} W(r, R) , \quad (31)$$

where

$$W(r, R) \equiv W\left(r + \frac{R}{2}, r - \frac{R}{2}\right) = W(x, y) , \quad (32)$$

with $r \equiv (x + y)/2$ and $R \equiv x - y$ denoting the center-of-mass and relative coordinates, respectively, and R being the canonical conjugate to the momentum p (as before r, p , etc., denote four vectors, and $a \cdot b \equiv a_\mu b^\mu$). The equations of motion for the Wigner transforms $\mathcal{W}(r, p)$ are now obtained [19] under the assumption that the Green functions and self-energies $W(r, R)$ can be approximated by a gradient expansion in r up to first order:

$$W(r + R, R) \simeq W(r, R) + R \cdot \frac{\partial}{\partial r} W(r, R) . \quad (33)$$

This assumption implies a restriction to quasi-homogenous or moderately inhomogenous systems, such that the Green functions vary only slowly with r . In homogenous systems,

such as the vacuum, translation invariance dictates that the dependence on r drops out entirely, and the Wigner transforms then coincide with the momentum-space Fourier transforms of the Green functions and self energies. Although we will in the present paper consider the evolution of a fragmenting jet system in vacuum, the subsequent formulation is tailored to apply also to more general translation *non*-invariant situations in moderately inhomogenous media.

The Dyson-Schwinger equations (28) can now be converted into kinetic equations by performing the Wigner transformation (31) for all Green functions and self energies, and using (33). One arrives at two distinct equations for each of the Wigner transforms \mathcal{S} , \mathcal{D} and Δ ($\tilde{\Delta}$), with rather different physical interpretations: (i) a *transport equation*, and (ii) a *constraint equation*. The *transport equations* are

$$\begin{aligned} p \cdot \partial_r \mathcal{S}_{ij}(r, p) &= \frac{1}{2} \delta_{ij} \gamma \cdot \partial_r + \frac{1}{4} (\gamma \cdot p + \Sigma) \mathcal{F}_{ij}^{(+)} + \frac{i}{8} \gamma \cdot \partial_r \mathcal{F}_{ij}^{(-)} \\ p \cdot \partial_r \mathcal{D}_{ab}^{\mu\nu}(r, p) &= \frac{1}{4} \mathcal{G}_{ab}^{\mu\nu (+)} \\ p \cdot \partial_r \Delta(r, p) &= -\frac{1}{4} \mathcal{H}^{(+)} , \end{aligned} \quad (34)$$

whilst the *constraint equations* are

$$\begin{aligned} \left[\left(p^2 - \frac{1}{4} \partial_r^2 \right) \delta_{ik} - \Sigma_{ik}^2(r, p) \right] \mathcal{S}_{kj}(r, p) &= \delta_{ij} (\gamma \cdot p + \Sigma) + \frac{i}{4} (\gamma \cdot p + \Sigma) \mathcal{F}_{ij}^{(-)} - \frac{1}{8} \gamma \cdot \partial_r \mathcal{F}_{ij}^{(+)} \\ \left[g_{\sigma}^{\mu} \left(p^2 - \frac{1}{4} \partial_r^2 \right) \delta_{ac} - \Pi_{\sigma, a, c}^{\mu}(r, p) \right] \mathcal{D}_{cb}^{\sigma\nu}(r, p) &= -\delta_{ab} \left(g_{\mu\nu} - \mathcal{E}^{\mu\nu} \right) + \frac{i}{4} \mathcal{G}_{ab}^{\mu\nu (-)} \\ \left[p^2 - \frac{1}{4} \partial_r^2 + \Xi(r, p) \right] \Delta(r, p) &= 1 - \frac{i}{4} \mathcal{H}^{-} . \end{aligned} \quad (35)$$

The equations for $\tilde{\Delta}$ are formally identical to those of Δ . The operator functions \mathcal{F} , \mathcal{G} , and \mathcal{H} ($\tilde{\mathcal{H}}$), which include the effects of spatial inhomogenities, are given by ($\partial_r^{\mu} \equiv \partial/\partial r^{\mu}$, $\partial_p^{\mu} \equiv \partial/\partial p^{\mu}$):

$$\begin{aligned} \mathcal{F}_{ij}^{(-)} &= \left([\partial_p^{\mu} \Sigma, \partial_{\mu}^r \mathcal{S}]_{-} - [\partial_r^{\mu} \Sigma, \partial_{\mu}^p \mathcal{S}]_{-} \right)_{ij} & \mathcal{F}_{ij}^{(+)} &= \left(\{ \partial_p^{\mu} \Sigma, \partial_{\mu}^r \mathcal{S} \}_{+} - \{ \partial_r^{\mu} \Sigma, \partial_{\mu}^p \mathcal{S} \}_{+} \right)_{ij} \\ \mathcal{G}_{ab}^{\mu\nu (-)} &= \left([\partial_p^{\mu} \Pi, \partial_{\mu}^r \mathcal{D}]_{-} - [\partial_r^{\mu} \Pi, \partial_{\mu}^p \mathcal{D}]_{-} \right)_{ab}^{\mu\nu} & \mathcal{G}_{ab}^{\mu\nu (+)} &= \left(\{ \partial_p^{\mu} \Pi, \partial_{\mu}^r \mathcal{D} \}_{+} - \{ \partial_r^{\mu} \Pi, \partial_{\mu}^p \mathcal{D} \}_{+} \right)_{ab}^{\mu\nu} \\ \mathcal{H}^{-} &= [\partial_p^{\mu} \Xi, \partial_{\mu}^r \Delta]_{-} - [\partial_r^{\mu} \Xi, \partial_{\mu}^p \Delta]_{-} & \mathcal{H}^{+} &= \{ \partial_p^{\mu} \Xi, \partial_{\mu}^r \Delta \}_{+} - \{ \partial_r^{\mu} \Xi, \partial_{\mu}^p \Delta \}_{+} . \end{aligned} \quad (36)$$

Eqs. (34) and (35) are our general master equations. The physical significance [19] of the transport equations (34) and the constraint equations (35) is that the former essentially

describe the space-time evolution of the Wigner transforms, whereas the constraint equations describe the “orthogonal” evolution in momentum space, and express a normalization condition imposed by unitarity and the renormalization group. In order to relate these operator equations to physically-relevant (observable) quantities, we define the *Wigner operators* $\hat{F}_\alpha(r, p)$ ($\alpha \equiv q, g, \chi, U$) in terms of the operators \mathcal{S} , \mathcal{D} , Δ , $\tilde{\Delta}$ and the self energies Σ , Π , Δ , $\tilde{\Delta}$ as follows:

$$\begin{aligned}
i\mathcal{S}_{ij}(r, p) &= \delta_{ij} (\gamma \cdot p + \Sigma) (2\pi i) \delta(p^2 - \Sigma^2) \hat{F}_q(r, p) \\
i\mathcal{D}_{ab}^{\mu\nu}(r, p) &= \delta_{ab} \varepsilon^{\mu\sigma}(p, s) \varepsilon_{\sigma}^{\nu*}(p, s) (2\pi i) \delta(p^2 - \Pi) \hat{F}_g(r, p) \\
i\Delta(r, p) &= (2\pi i) \delta(p^2 - \Xi) \hat{F}_\chi(r, p) \\
i\tilde{\Delta}(r, p) &= (2\pi i) \delta(p^2 - \tilde{\Xi}) \hat{F}_U(r, p) .
\end{aligned} \tag{37}$$

Then, by tracing over color and spin polarizations, and taking the expectation values (or, in a medium, the ensemble average) of these Wigner operators, one obtains the scalar functions

$$F_\alpha(r, p) \equiv F_\alpha(t, \vec{r}; \vec{p}, p^2 = M_\alpha^2) \quad (\alpha = q, g, \chi, U) \tag{38}$$

with

$$\begin{aligned}
F_q(r, p) &= \langle \text{Tr}[\mathcal{S}(r, p)] \rangle , & M_q^2 &= \Sigma^2(r, p) \\
F_g(r, p) &= \langle \text{Tr}[\mathcal{D}(r, p)] \rangle , & M_g^2 &= \Pi(r, p) \\
F_\chi(r, p) &= \langle \Delta(r, p) \rangle , & M_\chi^2 &= \Xi(r, p) \\
F_U(r, p) &= \langle \text{Tr}[\tilde{\Delta}(r, p)] \rangle , & M_U^2 &= \tilde{\Xi}(r, p) .
\end{aligned} \tag{39}$$

The c -number functions $F_\alpha(r, p)$ are the quantum-mechanical analogues of the classical phase-space distributions that measure the number of particles at time t in a 7-dimensional phase-space element $d^3r d^4p$. Due to the effects of the self energies, three-momentum and energy are generally independent variables, because the quanta can be off mass shell, i.e., for zero rest masses, $E^2 = \vec{p}^2 + M_\alpha^2 \neq \vec{p}^2$, where M_α^2 , eq. (39), represents the off-shellness due to the self and mutual interactions of the quanta ($M^2 = 0$ for on-shell particles). In contrast to the classical propagation of on-shell particles, the Wigner functions (37) incorporate the quantum “Zitterbewegung” even in the absence of interactions with other particles. These spatial fluctuations arise from the combination $p^2 - \partial_r^2/4$ acting on the Wigner operators in

(35), and account for the uncertainty in spatial localization of a quantum particle due to its momentum that is determined by the particle's self interaction. The self-consistent solution of the transport and constraint equations (34) and (35) therefore corresponds to summing over all possible quantum paths r in space-time with fluctuations in energy-momentum p , constrained by the uncertainty principle [19]. This simultaneous evolution in r and p of the Wigner functions F_α is illustrated in Fig. 4.

3.3 Macroscopic quantities

The functions F_α , eq. (38), contain the microscopic information that is required for the statistical description of the time evolution of a many-particle system in complete phase space [24]. Depending on the physical situation under consideration, one starts from specified initial distributions at $t = t_0$ and follows the time evolution of the phase-space densities $F_\alpha(r, p)$ according to the master equations (34) and (35). At any time $t > t_0$, $F_\alpha(r, p)$ reflects the state of the system around \vec{r} and \vec{p} . One can then calculate, in a Lorentz-invariant manner, directly from the microscopic densities F_α , the relevant macroscopic quantities that are related to observables. Relativistic transport theory [25] relates physical quantities to phase-space integrals over products of combinations of four-momenta or tensors and the particle distributions. Specifically, using (37), performing the traces over color and spin indices where necessary, and taking the ensemble average, one obtains the local space-time-dependent particle currents n_α and the corresponding energy-momentum tensors $T_\alpha^{\mu\nu}$ for the different particle species $\alpha = q, \bar{q}, g, \chi, U$, which are given by [24]

$$n_\alpha^\mu(r) = \int d\Omega_\alpha p^\mu F_\alpha(p, r), \quad T_\alpha^{\mu\nu}(r) = \int d\Omega_\alpha p^\mu p^\nu F_\alpha(r, p), \quad (40)$$

where $d\Omega_\alpha = \gamma_\alpha dM^2 d^3p / (16\pi^3 p^0)$, the γ_α are degeneracy factors for the internal degrees of freedom (color, spin, etc.), M_α measures the amount by which a particle α is off mass shell as a result of the self energy terms in (34), (35), and $p^0 \equiv E = +\sqrt{\vec{p}^2 + M_\alpha^2}$. These macroscopic quantities can be written in Lorentz-invariant form by introducing for each species α the associated matter flow velocity $u_\alpha^\mu(r)$, defined as a unit-norm time-like vector at each space-time point, $(u_\mu u^\mu)_\alpha = 1$. A natural choice is e.g. $u_\alpha^\mu = n_\alpha^\mu / \sqrt{n_{\nu\alpha} n_\alpha^\nu}$. By contracting the quantities (40) with the local flow velocities u_α^μ , one can now obtain corresponding invariant scalars of particle density, pressure, and energy density, for each particle

species α individually. For instance, in the absence of viscosity:

$$\begin{aligned} n_\alpha(r) &= n_{\mu\alpha}(r) u_\alpha^\mu(r) \\ P_\alpha(r) &= -\frac{1}{3} T_{\mu\nu,\alpha}(r) \left(g^{\mu\nu} - u_\alpha^\mu(r) u_\alpha^\nu(r) \right) \\ \varepsilon_\alpha(r) &= T_{\mu\nu,\alpha}(r) u_\alpha^\mu(r) u_\alpha^\nu(r) \quad . \end{aligned} \tag{41}$$

Due to the scalar character of these quantities, they provide local, Lorentz-invariant measures of the many-particle system. It is left to convenience in which Lorentz frame the calculation is performed, but in general it is considerably simplified in the local rest frame of the matter where $u^\mu = (1, \vec{0})$. The total number and the free energy of the particles at a given time can then be obtained by integrating over position space.

4. PARTON-HADRON CONVERSION OF FRAGMENTING JET SYSTEMS

The preceding kinetic formulation allows us now to apply the conceptual ideas of the effective field theory of Sec. 2 to the dynamics of parton-hadron conversion in rather general situations. In accord with the formalism of Sec. 2, the parton-hadron transition can be visualized as the conversion of high-momentum colored quanta of the fundamental quark and gluon fields into color-neutral composite states that correspond to local excitations of the condensate fields χ and U embedded in the physical vacuum.

Ultimately, we would like to address the dynamics of the (non-equilibrium) QCD phase transition in finite-temperature systems. Here, however, we will as a first application study a much simpler system, namely the fragmentation of a $q\bar{q}$ jet system with its emitted bremsstrahlung gluons, and describe the evolution of the system as it converts from the parton phase to the hadronic phase (illustrated in Fig. 5). A time-like virtual photon in an e^+e^- annihilation event with large invariant mass $Q \gg \Lambda_{QCD}$ ($\Lambda_{QCD} = 200 - 400$ MeV), corresponding to a very small initial size $L \ll L_c$ ($L_c = 0.5 - 1$ fm), is assumed to produce a $q\bar{q}$ pair which initiates a cascade of sequential gluon emissions. The early stage is characterized by emission of “hot” gluons far off mass shell in the perturbative vacuum. Subsequent gluon branchings yield “cooler” gluons with successively smaller virtualities, until their mutual separation approaches $L \approx L_\chi$. As is evident from the previous Fig. 2, this point characterizes the beginning of the transition, because the partons can now tunnel through the developing potential barrier and form color-singlet composite states, which

represent the particle excitations of the scalar long-range χ field. These “pre-hadronic” excitations must then convert into physical hadronic states – either excited gluonic states, or, via coupling to the U field, quark-antiquark meson excitations – and subsequently decay into low-mass hadrons.

4.1 General concept

As stressed in Sec. 2, the phenomenological color-singlet function χ represents the effect of the long-range order of the non-perturbative vacuum, so that the formation of a color-neutral parton cluster - or bubble - can be interpreted as a domain structure immersed in the medium of the non-perturbative vacuum. In quantum field theory such stable field configurations arise as *classical* soliton solutions of the equations of motion [9, 26]. On the other hand, it is well known that QCD exhibits the so-called ‘preconfinement’ property [27] already on the perturbative level, which is the tendency of the gluons and quarks produced in parton cascades to arrange themselves in color-singlet clusters with limited extension in phase space. It is therefore natural to suppose that these clusters, or bubbles, are the basic ‘pre-hadronic’ units out of which hadrons arise non-perturbatively.

Thus, the kinetic evolution of the system develops in three stages: parton multiplication, parton-cluster conversion, and cluster decay into hadrons. It is clear that in this approach the conversion process is a local, microscopic mechanism, that proceeds earlier or later at different points in space, depending on the local density of partons and their nearest-neighbour separation L , as defined by eq. (3). Thus, in order to trace the full dynamics, it is necessary to follow the evolution of the particle distributions in real time using the kinetic framework of Sec. 3. In accord with the above picture, we will now proceed in several steps, starting from the master equations (34) and (35): (i) employ a separation of a coherent (mean) field part and a contribution from quantum excitations for the composite fields χ and U , (ii) fix a specific, ghost-free gauge for the gluon fields that is most convenient for our purposes, (iii) treat the evolution of the high-momentum quarks and gluons perturbatively in the presence of the coherent field χ .

(i) According to our interpretation of oscillations about the minimum of the potential at χ_0, U_0 as physical excitations of the coherent fields χ and U , we separate in a standard way [28] the classical field configuration at the minimum of $\mathcal{V}_{\chi=\chi_0}$ in Fig. 2, from the quantum

fluctuations around this minimum. We represent $\chi = \bar{\chi} + \hat{\chi}$ and $U = \bar{U} + \hat{U}$, where $\bar{\chi}$, \bar{U} are c-number functions (the mean field parts), and $\hat{\chi}$, \hat{U} denote quantum operators (describing the excitations). The physics behind this separation is that the coupling of χ to ψ , $\bar{\psi}$, A^μ , as well as to U , will make the composite fields χ and U dynamical variables, so that the fluctuations around the mean fields $\bar{\chi}$ and \bar{U} will propagate and form collective excitations. Therefore the system is characterized (aside from the elementary fields ψ , $\bar{\psi}$, A^μ) by the mean fields, as well as by the collective excitations with their own energy spectrum and distribution. With this prescription we can treat the local interaction of the partonic fluctuations with the coherent field analogously to the familiar problem of quantum fields $(\psi, \bar{\psi}, A^\mu)$ interacting with a classical “external” field $(\bar{\chi})$, which converts the partons to color-singlet clusters or bubbles corresponding to excitations in the coherent field $(\hat{\chi})$. Specifically, in our approach the bubbles represent non-topological soliton configurations which are stable, classical solutions of the equations of motions, as have been studied for instance by Friedberg and Lee [9] and Coleman [26]. We do not include here the possible additional interactions between partons and bubbles, or among bubbles themselves.

(ii) It is convenient to work in a physical (axial) gauge [29, 30] for the gluon fields, generically given by choosing the gauge function $\xi_a(A)$ in (5) as

$$\xi_a(A) = -\frac{1}{2\alpha n^2} \partial_\lambda (n \cdot A_a) \partial^\lambda (n \cdot A_a), \quad (42)$$

where α is the gauge parameter, and n^μ is a constant vector with $n^2 \neq 0$. In particular, we will set $\alpha = 1$ which is known as the planar gauge. In contrast to covariant gauges where $\xi_a(A) = -1/(2\alpha)(\partial \cdot A_a)^2$, the class of gauges (42) is well known to have a number of advantages. It is ghost-free, i.e. the ghost field contribution in (19) decouples and drops out. Also, the so-called Gribov ambiguity is not present in this gauge. Another feature of (42) is that the gluon propagator involves only the two physical transverse polarizations, so that the equations (34) and (35) simplify considerably [19]. Furthermore, it allows for a rigorous resummation of the perturbative series at high energies in terms of the leading logarithmic contributions and consequently leads to a simple probabilistic description of the perturbative parton evolution within the (Modified) Leading Log approximation (MLLA) [31, 32] in QCD.

(iii) We will evaluate iteratively the 2-point Green functions \mathcal{S} and \mathcal{D} of quarks and gluons,

respectively, in the one-loop approximation in the framework of “jet calculus” [33], using the MLLA techniques of coherent parton evolution including soft-gluon interference [31]. The associated quark and gluon self energies Σ and Π include both the one-loop quark-gluon self interaction through real and virtual emission and absorption, and the effective interaction with the confining background field $\bar{\chi}$ [8]. Similarly, the self-energy Ξ of the χ field embodies the self interaction and the coupling to the U field, as contained in the effective potential (11), as well as contributions from quark and gluon recombination to χ excitations. Correspondingly, the function $\tilde{\Xi}$ of the U field incorporates its self interaction and the interaction with the χ field.

4.2 The kinetic equations for real-time evolution in phase space

As a consequence of the prescriptions (i)-(iii), and of exploiting in the present $e^+e^- \rightarrow \text{hadrons}$ case the special property of translation invariance of the parton evolution in the perturbative vacuum, one finds after a lengthy calculation [19] that the transport equations (34) and the constraint equations (35) can be combined in a single set of coupled integro-differential equations for the phase-space densities $F_\alpha(r, p)$ defined by (37) and (38). Introducing the usual light-cone variables

$$p^\mu = (p^+, p^-, \vec{p}_\perp), \quad p^\pm = p_0 \pm p_z, \quad \vec{p}_\perp = (p_x, p_y) \quad (43)$$

and

$$x = \frac{p^+}{Q}, \quad p_\perp = \sqrt{p_x^2 + p_y^2}, \quad p^2 = p_\mu p^\mu. \quad (44)$$

where Q is the hard scale of the initial $q\bar{q}$ pair created by the photon, and $r \equiv r^\mu = (t, \vec{r})$, we write

$$F_\alpha \equiv F_\alpha(r, p) = F_\alpha(t, \vec{r}; x, p_\perp^2, p^2). \quad (45)$$

The kinetic equations which one obtains from the transport equations (34) by implementing the constraints (35) can now be summarized compactly as follows (see Fig. 6):

$$\hat{\mathcal{K}} F_q = + \hat{A}_q^{qg} F_q + \hat{A}_g^{q\bar{q}} F_g - \hat{B}_{qg}^{q\chi} F_q F_g - \hat{B}_{q\bar{q}}^{\chi\chi} F_q F_{\bar{q}} \quad (46)$$

$$\hat{\mathcal{K}} F_g = + \hat{A}_g^{gg} F_g - \hat{A}_g^{q\bar{q}} F_g + \sum_f \hat{A}_q^{gq} F_{q+\bar{q}} - \hat{B}_{gg}^{\chi\chi} F_g F_g - \sum_f \hat{B}_{gq}^{\chi q} F_g F_{q+\bar{q}} \quad (47)$$

$$\hat{\mathcal{K}} F_\chi = + \hat{C}_{gg}^{\chi\chi} F_g F_g + \sum_f \hat{C}_{gq}^{\chi q} F_g F_{q+\bar{q}} + \sum_f \hat{C}_{q\bar{q}}^{\chi\chi} F_q F_{\bar{q}} - \hat{D}_\chi^U F_\chi - \hat{E}_\chi^h F_\chi \quad (48)$$

$$\hat{\mathcal{K}} F_U = + \hat{D}_\chi^U F_\chi - \hat{E}_U^h F_U, \quad (49)$$

where we have abbreviated $F_{q+\bar{q}} \equiv F_q + F_{\bar{q}}$, which in the present case is equal to $2F_q$, and the \sum_f means summing over quark flavors $f = u, d, s, \dots$. The left-hand sides of these equations describe the propagation of the particles in the presence of the mean field, whereas the terms on the right-hand sides represent the effects of particle creation, annihilation, and recombination. The operator $\hat{\mathcal{K}}$ on the left-hand sides is given by

$$\hat{\mathcal{K}} F_\alpha \equiv \left[p_\mu \partial_r^\mu + (\overline{M}_\alpha \partial_r^\mu \overline{M}_\alpha) \partial_\mu^p \right] F_\alpha, \quad (50)$$

with the first term describing the free propagation and the second term reflecting the effect of the mean field (Fig. 6a). The functions \overline{M}_α are the mean-field parts of the self energies M_α defined in (39). On the right-hand side the quantities $\hat{I}_{a_1, a_2, \dots}^{b_1, b_2, \dots}$ (where $\hat{I} = \hat{A}, \hat{B}, \dots$) represent integral operators that incorporate the effects of the self energies in terms of the relevant amplitudes for the various processes $a_1, a_2, \dots \rightarrow b_1, b_2, \dots$, and that act on the phase-space densities to their right (Fig. 6b). These coupled equations reflect a probabilistic interpretation of the evolution in terms of successive branching and recombination processes, in which the changes of the particle distributions on the left-hand sides are governed by the balance of gain (+) and loss (−) terms on the right-hand sides. The different terms on the right-hand sides of eqs. (46)-(49), the contributions to the gain and loss of particles, fall into three categories:

- (a) Parton multiplication through emission processes $q \rightarrow qg$, $g \rightarrow gg$ and $g \rightarrow q\bar{q}$;
- (b) Parton cluster formation through recombinations $q\bar{q} \rightarrow \chi\chi$, $qg \rightarrow q\chi$, $gg \rightarrow \chi\chi$;
- (c) Hadronic cluster decay either through direct conversion of the formed scalar χ excitations into hadrons h through $\chi \rightarrow h$, or via coupling to the pseudoscalar states $\chi \rightarrow U$, and the subsequent decay into hadrons, $U \rightarrow h$.

In the following subsections we explain these contributions in detail.

4.3 Parton multiplication

The integral operators \hat{A} in the quark and gluon evolution equations (46) and (47) represent the changes of the parton distributions in phase space due to the perturbative cascade evolution. Explicitly,

$$\begin{aligned} \hat{A}_q^{qq} F_q &= \lambda_\chi \int_0^1 dz \left[\frac{1}{z} F_q \left(r; \frac{x}{z}, zp_\perp^2, zp^2 \right) - F_q(r; x, p_\perp^2, p^2) \right] \gamma_{q \rightarrow qq}(z, \epsilon) a_q(z, p^2) \\ \hat{A}_g^{q\bar{q}} F_g &= \lambda_\chi \int_0^1 \frac{dz}{z} F_g \left(r; \frac{x}{z}, zp_\perp^2, zp^2 \right) \gamma_{g \rightarrow q\bar{q}}(z, \epsilon) a_g(z, p^2) \end{aligned}$$

$$\begin{aligned}
\hat{A}_g^{gg} F_g &= \lambda_\chi \int_0^1 dz \left[\frac{1}{z} F_g \left(r; \frac{x}{z}, zp_\perp^2, zp^2 \right) - \frac{1}{2} F_g(r; x, p_\perp^2, p^2) \right] \gamma_{g \rightarrow gg}(z, \epsilon) a_g(z, p^2) \\
\hat{A}_g^{q\bar{q}} F_g &= \lambda_\chi n_f(p^2) F_g(r; x, p_\perp^2, p^2) \int_0^1 dz \gamma_{g \rightarrow q\bar{q}}(z, \epsilon) a_g(z, p^2) \\
\hat{A}_q^{gq} F_{q+\bar{q}} &= \lambda_\chi \int_0^1 \frac{dz}{z} F_{q+\bar{q}} \left(r; \frac{x}{z}, zp_\perp^2, zp^2 \right) \gamma_{q \rightarrow gq}(z, \epsilon) a_q(z, p^2) .
\end{aligned} \tag{51}$$

Here $\lambda_\chi \equiv \lambda_\chi(\chi(r)) = 1 - (\chi/\chi_0)^4 + O[(\chi/\chi_0)^6]$, and the function $a(z, p^2)$ is given by

$$a_{q,g}(z, p^2) := \frac{1}{2\pi} T_{q,g}(p^2) \alpha_s \left((1-z)p^2 \right) , \tag{52}$$

with a “life-time” factor $T_{q,g}(p^2)$ that expresses the probability for a parton of virtuality p^2 to decay (branch) within a time interval t in the laboratory frame,

$$T_{q,g}(p^2) = 1 - \exp \left[-\frac{t}{\tau_{q,g}(p^2)} \right] , \tag{53}$$

where $\tau(p^2) \propto E/p^2$ (explicit expressions can be found in Ref. [34]). Furthermore, α_s is the one-loop QCD coupling

$$\alpha_s(k^2) = \frac{12\pi}{(33 - 2n_f(k^2)) \ln [(k^2 + k_0^2) L_c^2]} , \tag{54}$$

and $n_f(k^2)$ is the effective number of quark flavors at k^2 ,

$$n_f(k^2) := \sum_f^{N_f} \sqrt{1 - \frac{4m_f^2}{k^2}} \theta \left(1 - \frac{4m_f^2}{k^2} \right) . \tag{55}$$

In (54) we have assumed the correspondence $L_c \simeq \Lambda_{QCD}^{-1}$ to the intrinsic perturbative QCD scale, and k_0 is a parameter that prevents a divergence when $k^2 \rightarrow L_c^{-2}$, and defines a maximum value $\alpha_s(0)$. We will determine k_0 in Sec. 5 from the total parton multiplicity. The functions $\gamma(z, \epsilon)$ are analogous to the standard branching kernels in the MLLA [29]. Note that the 4-gluon vertex does not contribute in the MLLA in the gauge (42), because it is kinematically suppressed. As a consequence, the effect of the couplings $\kappa_L(\chi)$ and $\mu(\chi)$, eqs. (16) and (17), on the parton evolution reduces to 2-parton recombinations into color-singlet clusters – the terms proportional to \hat{B}, \hat{C} which will be given below.

The branching kernels $\gamma_{a \rightarrow bc}(z)$ are the familiar energy distributions for the branching $a \rightarrow bc$ with $z = x_b/x_a$ and $1-z = x_c/x_a$ the energy fractions of daughter partons:

$$\gamma_{q \rightarrow qg}(z, \epsilon) = C_F \left(\frac{1+z^2}{1-z+\epsilon} \right)$$

$$\begin{aligned}
\gamma_{q \rightarrow gq}(z, \epsilon) &= C_F \left(\frac{1 + (1-z)^2}{z + \epsilon} \right) \\
\gamma_{g \rightarrow gg}(z, \epsilon) &= 2C_A \left(\frac{z}{1-z+\epsilon} + \frac{1-z}{z+\epsilon} + z(1-z) \right) \\
\gamma_{g \rightarrow q\bar{q}}(z, \epsilon) &= \frac{1}{2} \left(z^2 + (1-z)^2 \right) ,
\end{aligned} \tag{56}$$

where $C_F = (N_c^2 - 1)/(2N_c) = 4/3$, $C_A = N_c = 3$. In the denominator of $\gamma_{q \rightarrow gq}$ and $\gamma_{g \rightarrow gg}$, there appears the function

$$\epsilon = \frac{p'^2 n^2}{4(p \cdot n)^2} \propto \frac{p_\perp^2}{p_z^2} , \tag{57}$$

where p (p') is the momentum of the mother (daughter) parton and p_\perp the relative transverse momentum of the daughter partons with respect to the mother. It arises here as a consequence of the constraint equations (35) which determine spatial uncertainty associated with the off-shellness of the partons. It effectively cuts off small-angle gluon emission by modifying the free gluon propagator $\propto z_g^{-1}$ to the form $(z_g + \epsilon)^{-1}$ (where $z_g = z$ or $z_g = 1 - z$) when $p_\perp/p_z = O(1)$, that is, in branching processes with large space-time uncertainty. This ensures that the two daughter partons can be resolved as individual quanta only if they are separated sufficiently by $\Delta r_\perp \propto 1/p_\perp$ in position space, in accord with the uncertainty principle. Note that ϵ can be neglected in the terms $\propto (z_g + \epsilon)^{-1}$ in (56) for energetic gluon emission ($z_g \rightarrow 1$), but is essential in the soft regime ($z_g \rightarrow 0$). The effect of ϵ has been shown [29, 35] to result in a natural regularization of the infra-red-divergent behaviour of the branching kernels (56), due to destructive gluon interference which becomes complete in the limit $z_g \rightarrow 0$.

4.4 Parton cluster (bubble) formation

The operators \hat{B}, \hat{C} in eqs. (46)-(48) represent the changes of the phase-space densities due to recombinations of two partons at r and r' to color-neutral clusters, or bubbles that arise as non-trivial structures in the vacuum because of the confinement mechanism. Their formation is determined, in analogy to the finite-temperature QCD phase transition [14], by the probability for tunnelling through the potential barrier of \mathcal{V} between $\chi = 0$ and $\chi = \chi_c$ in Fig. 2, which separates perturbative and non-perturbative vacua. The associated rate of bubble formation around $L = L_c$ is generically given by an exponential probability distribution [36, 37],

$$\pi(L) = \pi_0(L) \left(1 - \exp[-\Delta F L] \right) , \tag{58}$$

where $\pi_0 = \text{const.} \ln(1-u)\theta(1-2u) + \theta(2u-1)$, with $u = \Delta F L$, modifies the small- L behaviour for which the exponential form is not appropriate. Here ΔF is the change in the free energy of the system that is associated with the conversion from partons to clusters. In our case (for baryon-free matter in general),

$$\Delta F = E_{vol} + E_{surf} = \frac{4\pi}{3} R^3(L) \Delta P(L) + 4\pi R^2(L) \sigma(L), \quad (59)$$

where $R(L)$ is the radius of the bubble depending on the parton separation. The first term is the volume energy determined by the difference of pressure in the perturbative and the non-perturbative vacuum,

$$\Delta P(L) = P_{qg}(L) - P_\chi(L). \quad (60)$$

The second term in (59) is the surface energy with the surface tension estimated to be

$$\sigma(L) = \int_0^{\chi_c} d\chi \sqrt{2\mathcal{V}(L)} \approx 2 \int_{\chi_{max}}^{\chi_c} d\chi \sqrt{2\mathcal{V}(L)} \quad (61)$$

where χ_c corresponds to the local minimum of \mathcal{V} at L_c and χ_{max} is the point of the local maximum of \mathcal{V} that separates unconfined and confined domains, as defined in Fig. 2.

A parton bubble is stable if $\partial\Delta F/\partial R = 0$, which leads to the condition for the stationary bubble radius,

$$R_c \equiv R(L_c) = \frac{2\sigma}{\Delta P} \Big|_{L=L_c} \quad (62)$$

When inserted in (59), this gives for (58)

$$\pi(L) = \pi_0(L) \left(1 - \exp \left[-\frac{4\pi}{3} R_c^2 \sigma_c L \right] \right) \quad (63)$$

with $\sigma_c \equiv \sigma(L_c)$. In accord with our definition (3), we interpret the space-time scale L as the characteristic inter-parton separation, that is, we define it in terms of the distance measure Δ_{ij} between two partons, labeled with indices a and b ,

$$\Delta_{ab} = \sqrt{r_{ab}^\mu r_{ab,\mu}}, \quad r_{ab} = r_a - r_b, \quad (64)$$

and identify L with the the minimum distance L_{ab} for a certain parton a to its next neighbour b :

$$L(r) = L_{ab} \equiv \min_b (\Delta_{a1}, \dots, \Delta_{ab}, \dots, \Delta_{an}). \quad (65)$$

Other measures are possible, e.g. $\Delta_{ab} = (1/x_{ab}^2 + 1/y_{ab}^2 + 1/z_{ab}^2 + 1/(\Delta t)^2)^{-1/2}$, but we find that the particular choice of Δ_{ab} is not crucial as long it provides a reasonable distance

measure. We choose (64), because it has the advantage that it is manifestly Lorentz-invariant and has a simple interpretation as the two partons' spatial separation in their center-of-mass frame.

We assume that the dominant contribution to bubble formation arises from 2-parton fusion and ignore recombinations of 3 or more partons. This is reasonable, unless the local parton density becomes so large that also the latter processes have a significant probability to occur. We take the same probability distribution $\pi(L)$ for the various types of configurations, since it depends only on the 'color- and flavor-blind' variable L , i.e. we set

$$\pi(r, r') = \pi(L) \equiv \pi_{gg \rightarrow \chi\chi}(L) = \pi_{q\bar{q} \rightarrow \chi\chi}(L) = \pi_{gq \rightarrow \chi q}(L), \quad (66)$$

where L is given in terms of r and r' by (65). The various \hat{B} terms in (46) and (47) can then be expressed generically as:

$$\hat{B}_{ab}^{\chi c} F_a F_b = F_a(r; x, p_\perp^2, p^2) \int d^3 r' \pi(r, r') \int d^4 p' F_b(r'; x', p_\perp'^2, p'^2) \quad (67)$$

where $a, b = q, \bar{q}, g$ and $c = \chi, q$, and $d^4 p' = dp_\perp'^2 dx'/x'$. Similarly the \hat{C} terms in (48) are given by:

$$\begin{aligned} \hat{C}_{ab}^{\chi c} F_a F_b &= \int d^3 r' \int d^3 r'' \pi(r', r'') \delta^3 \left(\vec{r} - \frac{\vec{r}' + \vec{r}''}{2} \right) \\ &\times \int d^4 p' d^4 p'' F_a(r'; x', p_\perp'^2, p'^2) F_b(r''; x'', p_\perp''^2, p''^2) \delta^4 \left(p - \frac{p' + p''}{2} \right) \end{aligned} \quad (68)$$

4.5 Hadronic cluster decay

The ensemble of clusters determined by the coupled equations (46)-(48) yields a continuous mass spectrum of color-singlet excitations with different flavor contents corresponding to the types of recombined partons. These states must then decay into physical hadronic states with a discrete mass spectrum. The invariant mass distribution of the formed clusters may be interpreted as a 'smeared out' version of the spectrum of primordial resonances formed in the early stages of the confinement mechanism [31]. It therefore seems reasonable to treat the fragmentation of these central clusters as a kind of averaged resonance decay which, as implied by our locality assumption, must be determined entirely by their invariant masses, flavors and total angular momenta. Each cluster in the resonance spectrum may

either represent a single hadron resonance that converts directly into a physical hadron with a definite mass, or else fragments through a two-body decay into a pair of final-state hadrons. From the particle spectra obtained in e^+e^- -annihilation experiments it appears that quasi-two-body final states are universally dominant, so that the latter possibility seems favored if kinematically allowed.

We adopt the cluster fragmentation scheme of Refs. [38, 39], however with some modification concerning heavy clusters. We assume that each cluster $C = \chi, U$ can decay by either one of the following mechanisms:

(i) If a cluster C is too light to decay into two hadrons, it is taken to represent the lightest single hadron (meson) h , corresponding to its partonic constituents, $C \rightarrow h$, with its mass shifted to the appropriate value by adjusting its energy through exchange with a neighbouring cluster.

(ii) If, however, a cluster is massive enough to decay, it decays isotropically in its rest frame into a pair of hadrons (mesons or baryons), $C \rightarrow h_1 + h_2$ according to the decay probability specified below.

Occasionally it occurs that a cluster comes out very heavy, in which case isotropic 2-body decay is not a reasonable mechanism any more. In this case we impose the constraint that, if a cluster is heavier than a critical threshold $M_{crit} = 4 \text{ GeV}$, then it is rejected and the two recombining partons of that potential cluster propagate on as individual quanta, and continue to participate in the parton cascade process, either until they have decreased their virtuality sufficiently, or until they recombine with a lower-mass partner.

To implement this scheme, we observe from eqs. (48) and (49) that the cluster-hadron transformation can proceed through the scalar channel $\chi \rightarrow h$, or via the pseudoscalar channel $\chi \rightarrow U \rightarrow h_1 h_2$, depending on the corresponding density of states with masses below the decaying cluster. We assume a Hagedorn [40] density of states

$$\rho_h(m) = c m^{-a} \exp\left(-\frac{m}{T_0}\right), \quad (69)$$

where c, a are constants and T_0 is the Hagedorn temperature with the typical values $c = 8m_\pi^2$, $a = 3$ and $T_0 = m_\pi$. The decay probability of a cluster with mass $m_C = \sqrt{p^2}$ to decay into a hadron state of mass $m'_h = \sqrt{p'^2}$ is then given by

$$\Gamma_{C \rightarrow h}(p, p') = \frac{1}{N_C(p^2)} T_C(p^2) \int_{m'_h = \sqrt{p'^2}}^{m_C = \sqrt{p^2}} dm \rho_h(m). \quad (70)$$

Here

$$N_C(p^2) = \int_{m_\pi}^{\sqrt{p^2}} dm \rho_h(m), \quad (71)$$

and in analogy to (53), $T_C(p^2)$ is a “life-time” factor giving the probability that a cluster of mass $m_C^2 = p^2$ decays within a time interval t in the laboratory frame,

$$T_C(p^2) = 1 - \exp\left[-\frac{t}{\tau_C(p^2)}\right], \quad (72)$$

where in this case we simply take $\tau_C(p^2) = E_C/p^2 = \gamma/m_C$ from the uncertainty principle. In order to find the value for the decay probability (70) for a given cluster of mass m_C , we sum over the possible decays for this cluster according to the particle data tables. The probability for a specific 2-body decay mode is taken to be a product of a flavor, a spin and a kinematical factor [38],

$$\Gamma_{C \rightarrow h_1 h_2}(m_C; m_1, m_2) := P_m(m_C, m_1 + m_2) P_s(j_1, j_2) P_k(m_C, m_1, m_2), \quad (73)$$

where $j_{1,2}$ ($m_{1,2}$) are the angular momenta (masses) of the two hadrons $h_{1,2}$. The factor

$$P_m(m_C, m_1 + m_2) = \left(1 + \frac{m_1^2 + m_2^2}{m_C^2}\right) \sqrt{1 - \frac{(m_1 + m_2)^2}{M_c^2}} \theta(m_C - m_1 - m_2) \quad (74)$$

is the two-body phase-space suppression function for the decay. The spin factor

$$P_s(j_1, j_2) = (2j_1 + 1) (2j_2 + 1) \quad (75)$$

takes into account the spin degeneracy with the allowed spins j_1 and j_2 of the two hadrons.

The kinematic factor

$$P_k(m_C, m_1, m_2) = \frac{\sqrt{\lambda(m_C^2, m_1^2, m_2^2)}}{m_C^2} \quad (76)$$

is the two-body phase-space factor, where $\lambda(a, b, c) = a^2 + b^2 + c^2 - 2(ab + ac + bc)$.

Thus, with the decay probability $\Gamma_{C \rightarrow h}$ of (70) evaluated in this fashion, the terms involving the \hat{D} and \hat{E} operators in the kinetic equations (48) and (49) can be expressed as

$$\begin{aligned} \hat{D}_\chi^U F_\chi &= F_\chi(r; x, p_\perp^2, p^2) \int dp'^2 \Gamma_{\chi \rightarrow U}(p^2, p'^2) \\ \hat{E}_\chi^h F_\chi &= F_\chi(r; x, p_\perp^2, p^2) \int dp'^2 \Gamma_{\chi \rightarrow h}(p^2, p'^2) \\ \hat{D}'_\chi^U F_\chi &= \int dp'^2 dp_\perp'^2 \frac{dx'}{x'} F_\chi(r; x, p_\perp'^2, p'^2) \Gamma_{\chi \rightarrow U}(p'^2, p^2) \\ \hat{E}'_U^h F_U &= F_U(r; x, p_\perp^2, p^2) \int dp'^2 \Gamma_{U \rightarrow h}(p^2, p'^2) \end{aligned} \quad (77)$$

4.6 Method of solution by Monte Carlo simulation

We can now solve the set of evolution equations (46)-(49) by means of a real-time simulation in full phase space using the computational methods of Ref. [38]. One starts from an initial phase-space density of partons, which in the case of a jet-initiating $q\bar{q}$ pair with invariant mass Q is

$$F_{q+\bar{q}}(t=0, \vec{r}; x, p_\perp^2, p^2) = \delta^3(\vec{r}) \delta(\vec{r}^2 - Q^2) \delta(x-1) \delta(p_\perp^2) \delta(p^2 - Q^2), \quad (78)$$

where we choose the $q\bar{q}$ center-of-mass frame as our reference frame, and we sum over all quark flavors f weighted with a factor $w_f = e_f^2/n_f(Q^2)\sqrt{1-4m_f^2/Q^2}\theta(Q^2-4m_f^2)$, that accounts for the electromagnetic charge and mass threshold of the initial $q\bar{q}$ pair produced by the photon (or Z^0).

The parton shower development is then followed in a cascade simulation (for details see [24, 38]) in the center-of-mass frame: The system of particles is evolved in discrete time steps, here taken as $\Delta t = 0.01 fm$, in coarse-grained 7-dimensional phase-space with cells $\Delta\Omega = \Delta^3 r \Delta^3 p \Delta M^2$. The partons propagate along classical trajectories until they interact, i.e., decay (branching) or recombine (cluster formation). Similarly, the formed clusters travel along straight lines until they decay into hadrons. The corresponding probabilities and time scales of interactions are sampled stochastically from the relevant probability distributions according to Secs. 4.3-4.5. At any time $t > 0$ we can extract the phase-space densities (38), $F_\alpha(t, \vec{r}, \vec{p}, p^2) = dN_\alpha(t)/d^3 r d^4 p$ of the particle species $\alpha = q, g, \chi, U$, and with these phase-space profiles we can then calculate, using the formulae (40) and (41), the associated local pressure $P(r)$, particle density $n(r)$ and energy density $\varepsilon(r)$ for each species individually, these being the quantities that characterize the macroscopic state of the system at t and \vec{r} .

With this concept, we can trace the space-time evolution of the parton-hadron conversion process self-consistently: at each time step, any “hot” off-shell parton is allowed to decay into “cooler” partons, with a probability determined by its virtuality and life time. Also in each step, every parton and its nearest spatial neighbor are considered as defining a fictitious space-time bubble with invariant radius L , as defined by (65). By comparing the local pressure of partons $P_{qg}(t, \vec{r}, L)$ with the pressure $P_\chi(t, \vec{r}, L)$ that such a pre-hadronic

bubble would create instead, we obtain the associated value of the conversion probability $\pi(L)$ which determines the cluster (bubble) formation rate explained in Sec. 4.5. If the partons do convert into a cluster, they disappear from a phase-space cell, and instead the composite cluster appears at the same space-time point, from which it propagates on. Otherwise the partons continue in their shower development. The final decay of each formed cluster into hadrons is simulated analogously, except that it does not require the comparison of pressures, but is determined by kinematics and the available phase space. This cascade evolution is followed until all partons have converted, and all clusters have decayed into final-state hadrons.

As an illustrative example, we show in Fig. 7 the time evolution of the particle density profiles of partons (Fig. 7a) and clusters (Fig. 7b) for a jet system with invariant mass $Q = 100$ GeV. It is evident how the system evolves in position space with respect to the center-of-mass of the two initial partons as a polar wave front (the pictures are symmetric in $r_\perp = \sqrt{r_x^2 + r_y^2}$), with the partons gradually converting to clusters. It is interesting that this local excitation of the vacuum due to the injection of the highly virtual dijet system, and the subsequent evolution, resemble very much the situation of a stone plunged into water, with a well-shaped “shock front” expanding isotropically in the center-of-mass frame.

5. PHENOMENOLOGY

In this Section we study the observable implications of our approach to parton-hadron conversion, and investigate its consistency with standard particle physics phenomenology.

5.1 Determination of the potential $V(\chi, U)$

We first need to specify the parameters of our approach. Recall that this phenomenological input is contained in the effective long-range potential $V(\chi, U)$, eq. (11), which combines with the dynamical contribution $\delta V(L, \chi)$ to the L -dependent potential $\mathcal{V}(L)$, eq. (21). As L varies, \mathcal{V} changes its shape, which affects the dynamical evolution of the system, and the latter in turn determines the further change of \mathcal{V} . Hence, the details of the dynamics are governed by the choice of parameters in V and thus \mathcal{V} . The crucial parameters are the bag constant B which defines the vacuum pressure $V(0)$ in the short-distance limit $L \rightarrow 0$, and χ_0 , the value of the condensate of χ in the long-distance regime. As indicated

in Fig. 2, as L increases, the changing form of $\mathcal{V}(L)$ is characterized by three distinct length scales: $L = L_\chi$, the point when partons begin to convert, $L = L_c$, when the pressures of partons and pre-hadronic clusters equal each other, and $L = L_0$, when the transition is completed.

We will fix B and χ_0 , which have well-defined physical interpretations, and then determine L_χ , L_c and L_0 . Although the values of B and χ_0 are not precisely known, there is agreement of various phenomenological determinations about their ranges: one expects [14] $B^{1/4} = (150 - 250)$ MeV and $\chi_0 = (50 - 200)$ MeV. In the following we adopt two representative parameter combinations:

$$\begin{aligned} B^{1/4} &= 230 \text{ MeV} & \chi_0 &= 200 \text{ MeV} \\ B^{1/4} &= 180 \text{ MeV} & \chi_0 &= 100 \text{ MeV} . \end{aligned} \quad (79)$$

Then, with the potential \mathcal{V} specified, we can determine the values of L_χ , L_c , L_0 from the Monte Carlo simulation of the evolution of the system as the scale L changes due to the particles' diffusion in phase space. The most interesting quantity is L_c , the point which is characterized by the equality of partonic and hadronic pressures. As explained in Sec. 4.6, we can compute the corresponding pressures P_{gg} and P_χ from the phase-space densities of partons and clusters, respectively. In analogy to Ref. [14], we represent (on dimensional grounds)

$$\begin{aligned} P_{gg}(r, L) &= a_{gg}(r, L) L^{-4} - B \\ P_\chi(r, L) &= a_\chi(r, L) L^{-4} - \mathcal{V}(L) , \end{aligned} \quad (80)$$

and, because $\mathcal{V}(\chi, L)|_{L=L_c} = \mathcal{V}(\chi_c, L_c) = 0$ (c.f. Fig. 2), we have

$$L_c = \left[\frac{a_{gg}(r, L_c) - a_\chi(r, L_c)}{B} \right]^{1/4} . \quad (81)$$

The dimensionless functions a_{gg} and a_χ are obtained from the numerical simulation and are shown in Fig. 8 as a function of time for the above two choices of B and χ_0 in the cases of $q\bar{q}$ and gg jet evolution with $Q = 10$ GeV and $Q = 100$ GeV. Plotted are the kinetic pressures $P(t, L) := a(t, L)L^{-4}$ (where $t \simeq \sqrt{L^2 + z^2}$) along the “shock front” of the jet profile which is seen in the previous Fig. 7. From Figs. 8a and 8b one observes that (i) the pressure evolution obviously depends on the type of the two jet-initiating partons: it

decreases more slowly for $q\bar{q}$ pairs of different flavors than for a gg pair, because gluons have a larger emission rate and therefore the two leading gluons evaporate their initial energy faster; (ii) the crossover point between the pressures P_{gg} and P_χ is rather insensitive to the choice of L_c ; (iii) the crossover is shifted away from $t = 0$ with increased jet energy Q ; (iv) at L_c the partonic pressure P_{gg} still exceeds P_χ , i.e. $a_{gg}(L_c) > a_\chi(L_c)$, consistent with (81). From this analysis, we find using the determining condition (81),

$$L_c = \begin{cases} 0.6 \text{ fm} & \text{for } B^{1/4} = 230 \text{ MeV} \\ 0.8 \text{ fm} & \text{for } B^{1/4} = 180 \text{ MeV} \end{cases}. \quad (82)$$

Directly associated with the scale L_c is the parton-cluster conversion probability (63), which is determined by the width of the potential wall between the two phases. It enters the kinetic equations via (67) and determines locally the time scale of the parton-to-cluster transition by the magnitude of the surface tension σ_c as given by (61). We find

$$\sigma_c^{1/3} = \begin{cases} 40 \text{ MeV} & \text{for } L_c = 0.6 \text{ fm} \text{ } (B^{1/4} = 230 \text{ MeV}) \\ 48 \text{ MeV} & \text{for } L_c = 0.8 \text{ fm} \text{ } (B^{1/4} = 180 \text{ MeV}) \end{cases}, \quad (83)$$

which by virtue of (63) fixes the cluster-formation probability $\pi(L)$. It is noteworthy that the above small values of the surface tension σ_c are in agreement with lattice QCD simulations [41]. and correspond to a weakly first-order transition at finite temperature, which is consistent with astrophysical constraints [42] on inhomogenities. This finding implies a rather rapid conversion of partons into color-singlet clusters (pre-hadrons), as is also evident from Fig. 8. This means that parton-hadron conversion is not dependent on the details of the interpolation functions $\kappa_L(\chi)$ and $\mu_L(\chi)$, as already advertised in Sec. 2.3, and has interesting consequences for the cluster size and mass distribution, as we will discuss below.

The value of L_χ , below which size only the perturbative vacuum of the pure parton phase can exist, is given by the point of inflection of the effective potential \mathcal{V} , when the local minimum at $\langle\chi\rangle \neq 0$ ceases to exist (c.f. Fig. 2). It turns out to be rather close to L_c ,

$$L_\chi \approx \begin{cases} 0.4 - 0.5 \text{ fm} & \text{for } L_c = 0.6 \text{ fm} \text{ } (B^{1/4} = 230 \text{ MeV}) \\ 0.6 - 0.7 \text{ fm} & \text{for } L_c = 0.8 \text{ fm} \text{ } (B^{1/4} = 180 \text{ MeV}) \end{cases}, \quad (84)$$

which is a consequence of the small values (83) for the surface tension σ_c , and indicates that the transition occurs very abruptly. Finally, we find that the scale L_0 , when the parton-cluster conversion is complete and no partons are left over, depends not only on L_c but also

on the initial jet energy Q . It gives an estimate for the time scale $\tau_0 \propto L_0$ of the global conversion process, and comes out rather long, namely for $L_c = 0.6 \text{ fm}$ we get $\tau_0 \approx 8.5$ (21) fm for $Q = 10$ (100) GeV, whilst for $L_c = 0.8 \text{ fm}$ the time scale is $\tau_0 \approx 10$ (26) fm for $Q = 10$ (100) GeV.

Immediate consequences of the values for B and χ_0 in (79) are the “critical temperature” for the phase transition in finite-temperature QCD,

$$T_c \equiv \left(\frac{9B}{4\pi^2} \right)^{1/4} = \begin{cases} 160 \text{ MeV} & \text{for } L_c = 0.6 \text{ fm} \text{ } (B^{1/4} = 230 \text{ MeV}) \\ 125 \text{ MeV} & \text{for } L_c = 0.8 \text{ fm} \text{ } (B^{1/4} = 180 \text{ MeV}) \end{cases}, \quad (85)$$

the characteristic mass scale of the lightest scalar glueball, given by [14]

$$m_\chi \equiv \sqrt{\left. \frac{\partial^2 V(\chi, 0)}{\partial \chi^2} \right|_{\chi=\chi_0}} = 4 \frac{\sqrt{B}}{\chi_0} = \begin{cases} 1.05 \text{ GeV} & \text{for } L_c = 0.6 \text{ fm} \\ 1.30 \text{ GeV} & \text{for } L_c = 0.8 \text{ fm} \end{cases}, \quad (86)$$

and, the estimate for the value of the gluon condensate (23),

$$G_0 = \frac{32}{9} B = \begin{cases} 1.25 \text{ GeV fm}^{-3} & \text{for } L_c = 0.6 \text{ fm} \\ 0.50 \text{ GeV fm}^{-3} & \text{for } L_c = 0.8 \text{ fm} \end{cases}. \quad (87)$$

The parameter values obtained above are summarized in Table 1. Both choices (79) of $B^{1/4}$ and χ_0 give reasonable results that are in the range of commonly-accepted phenomenology.

5.2 Cluster distributions and hadron spectra

Using the parametrizations of Table 1, we have investigated more quantitatively a number of typical features of the jet evolution, which we discuss now.

In Fig. 9 we show the total transverse momentum generated during the time evolution of the system in the center-of-mass of the initial jet pair:

$$p_\perp^{(\alpha)}(t) \equiv \int d^3r \int dx dp^2 dp_\perp^2 p_\perp F_\alpha(t, \vec{r}; x, p_\perp^2, p^2), \quad (88)$$

where α labels ‘partons’ or ‘clusters’, and $p_\perp \equiv \sqrt{p_x^2 + p_y^2}$. As before, we compare the cases $Q = 10$ (100) GeV and $L_c = 0.6$ (0.8) fm . At $t = 0$ we start with $p_\perp^{(\alpha)}(0) = 0$, because the two initial partons recede back-to-back along the z axis. Then, with progressing time, the jet evolution can roughly be divided into four stages: (i) a very short *hard stage* ($\lesssim 0.02$

fm), characterized by an explosive production of partons and consequently transverse momentum; (ii) a longer *shower stage* ($\approx 0.02 - 0.3 fm$) that essentially just causes diffusion in phase space with little additional entropy and transverse momentum production; (iii) a *conversion stage* ($\approx 0.3 - 5 fm$) which sets in when the partons start locally to form clusters; (iv) a *hadronization stage* ($\gtrsim 5 fm$) when the clusters start fragmenting into physical hadron states via cluster decay and resonances.

It is interesting to inspect the distribution of the cluster sizes and the invariant-mass spectrum of clusters, since these measures are essentially the only microscopic information (aside from the momentum spectrum) which is carried over from the partonic to the hadronic phase, and therefore determines directly the final-state hadron distributions. In Figs. 10 and 11 we show these distributions, for the two values of L_c and the two jet energies Q considered before.

From Fig. 10a it is obvious that the typical cluster radius is strongly peaked at a value slightly above L_c , with a very small width of about $10^{-1} fm$. Specifically, the average cluster size is $\langle R_{cl} \rangle = 0.62 (0.83) fm$ for $L_c = 0.6 (0.8) fm$. The narrow width of the cluster size distribution is a consequence of the smallness of the surface tension σ_c (83), which implies a very small surface energy to be overcome, and results in a jump in the tunnelling probability (58) around $L = L_c$. One also sees that there are a few clusters with radius smaller than L_c , a feature which arises from the fact that cluster formation sets in already at L_χ (c.f. Table 1), when there is a non-zero transition probability for partons to yield clusters by tunnelling through the potential barrier that begins to develop when $L > L_\chi$ (c.f. Fig. 2). A striking feature of the cluster mass spectrum shown in Fig. 10b is that it is insensitive to the choice of L_c . The spectrum is characterized by a strongly-damped exponential form at low mass ($M_{cl} \lesssim 3 GeV$), with a high-mass tail that extends substantially beyond 5 GeV. For both choices of L_c , the value for the average cluster mass is $\langle M_{cl} \rangle \simeq 1.2 GeV$, which is in qualitative agreement with the characteristic mass scale m_χ obtained in (86) as an estimate.

Figs. 11a and 11b display the corresponding size and mass distribution for the case when we impose the constraint mentioned in Sec. 4.3, that two partons cannot form a cluster if their invariant mass is above a maximum cluster mass M_{crit} , even if their mutual separation increases beyond L_c , where we chose $M_{crit} = 4 GeV$. In this case the two partons propagate

on as individual quanta until they have either radiated off further energy, or recombine with a less-energetic partner. Consequently, the cluster size distribution is shifted to larger radii, not however very significantly, because only a small fraction (typically less than 5 %) of the clusters are affected. At the same time, the mass distribution loses its high-mass tail and falls off considerably above 3 GeV, and the average cluster mass comes down substantially to $\langle M_{cl} \rangle \simeq 0.8$ GeV.

The most remarkable result of Figs. 10 and 11, however, is that the shapes of both the cluster size and cluster mass distribution are essentially independent of the jet energy, as well as of the initial 2-jet configuration, and therefore appear to be universal.

The decay of the spectrum of formed clusters into hadrons, simulated according to the Sec. 4.5, then yields the average particle multiplicities of final-state hadrons. It is interesting to look at the relation between parton and hadron multiplicities. The feature evident in Figs 10b and 11b, namely that the mass spectrum of color-singlet clusters is independent of the total jet energy, is in agreement with analytical predictions [31]. This implies that parton and hadron multiplicities should be proportional to each other at high energies, which is known as *local parton-hadron duality* [32]. Fig. 12 display our results for the total gluon and quark multiplicities $\langle n_{qg} \rangle = \langle n_g \rangle + \sum_f \langle n_q + n_{\bar{q}} \rangle$, as well as the ratios of charged hadrons to partons $\langle n_{ch} \rangle / \langle n_{qg} \rangle$, and of clusters to partons, $\langle n_{cl} \rangle / \langle n_{qg} \rangle$, as a function of jet energy Q . In Fig. 12a the calculated rise of $\langle n_{qg} \rangle$ is shown for the two choices of L_c . The smaller value of L_c gives a larger multiplicity because we identified L_c^{-1} with the scale Λ_{QCD} in α_s , eq. (54). From Fig. 12b one reads off, however, that the average number of clusters per parton is independent of L_c and of energy Q . As a consequence, the number of charged hadrons per parton is larger for larger L_c , because at any fixed Q and due to 4-momentum conservation, fewer partons yield more massive clusters which in turn decay in a larger number of low-mass hadrons. Most important, one sees that the ratio $\langle n_{ch} \rangle / \langle n_{qg} \rangle$ is only weakly energy-dependent for $Q \gtrsim 30$ GeV, in accord with the hypothesis of local parton-hadron duality: it rises over this range by less than 10% and appears to saturate asymptotically, approaching a constant of ≈ 1.6 (1.7) for $L_c = 0.6$ (0.8) fm .

The resulting average multiplicity of charged hadrons as it rises with Q is shown in Fig. 13a together with experimental data [45, 46]. In order to obtain the correct overall normalization, we fitted the the infrared regulator k_0 entering α_s , eq. (54), to give the

measured total charged multiplicity at $Q = 91$ GeV for $L_c = 0.8$ fm. The required value is $k_0 = 0.5$ GeV which implies $\alpha_s(0) \approx 0.8$. With this adjustment we then obtain in Fig. 13b the momentum spectra of charged hadrons with respect to the variable $\ln(1/x)$, where $x = 2E/Q$ is the particle energy normalized to the total energy Q . The spectra clearly exhibit the well known ‘hump-back plateau’ [32]. The good agreement of the simulation with experimental spectra is another indicator of the aforementioned local parton-hadron duality. The result is not surprising, since the simulation incorporates the *coherent* parton shower evolution [38] based on the soft-gluon interference properties of the MLLA, which cause this hump-back plateau with its depletion at small x . Because in our approach cluster formation and subsequent cluster decay involve no momentum dependence, but are solely described by the space-time separation of partons, the parton momentum spectra in x are mapped almost unaltered onto the hadron distributions. We also conclude, that the comparisons in Fig. 13 do not indicate any clear preference for one value of B or L_c over the other. However, as we will discuss in Sec. 5.3, an indication may be drawn from Bose-Einstein correlations among produced hadrons.

An example of the composition of the final hadron yield in terms of different particle species is given in Table 2, where we compare the result of our simulation of e^+e^- annihilation events at $Q = 34$ GeV with measured particle multiplicities [47]. The remarkable agreement is in accord with the presumption that the different particle yields are essentially determined by the available phase space and the density of hadron states, and not by more complex mechanisms. Further experimental constraints by more sensitive measures of event shapes such as thrust, sphericity, etc., may be investigated, but it is evident from the results shown that our approach yields an overall satisfactory description that withstands confrontation with experiment, and encourages us to study more complex reactions in the near future.

5.3 The Bose-Einstein effect

From Figs. 10 and 11 we can conclude that the distribution of formed clusters clearly resembles the picture of *preconfinement* [27], which is the tendency of partons produced during the cascade evolution to arrange themselves in color-singlet clusters with limited extension in both position and momentum space. Since the clusters are the basic units within which the final-state hadrons arise, the ensemble of clusters in phase space, as it

builds up with time, can be interpreted as a particle emission source with a space-time distribution that is determined by the preceding parton evolution. This notion allows us to directly relate the dynamics of cluster formation to the well-known Bose-Einstein effect [48], which corresponds to an enhancement in the production rate of identical bosons (in our case mainly pions) emitted from similar regions in space and time, arising from the imposition of Bose symmetry. Enhancements in the mass spectrum of *same-sign* pion pairs have been seen clearly in e^+e^- -data (for a review see e.g. [44]). Let us briefly recall that the Bose symmetry imposed on the production amplitude of identical particles from a distribution of sources leads to an interference term in the squared amplitude which is only observable if the sources are incoherent. From the analysis of e^+e^- -data one finds [44] that the Bose-Einstein effect is reasonably described by a spherically-symmetric space-time distribution of sources with Gaussian form

$$\rho(r) = \rho(0) \exp\left(-\frac{r^2}{2\sigma_\rho^2}\right), \quad (89)$$

where σ_ρ is a radius parameter. Such a source leads to an enhancement due to interference caused by the identical-particle effect, relative to the rate with no interference,

$$b(q) = 1 + \lambda_\rho \exp\left(-\sigma_\rho^2 q^2\right), \quad (90)$$

where $q^2 = m_{\pi\pi}^2 - 4m_\pi^2$, and $m_{\pi\pi} = \sqrt{(p_1 + p_2)^2}$ is the invariant mass of the emitted pion pair. The degree of incoherence of the source is measured by λ_ρ ($=1$ for complete incoherence, and $=0$ for complete coherence), σ_ρ measures the source size in fm , or alternatively, σ_ρ^{-1} measures the range of enhancement with respect to q in GeV .

To observe an enhancement in q amongst identical particles, one must compare the particle distributions with corresponding spectra in the complete absence of Bose symmetry. Thus, in order to get an estimate of the magnitude of enhancement implied by our hadronization picture, we proceed as follows. First we evaluate the pion distributions resulting from a simulation which does not include the Bose-Einstein effect. Then we repeat the calculation, but now imposing Bose symmetrization on same-sign pion pairs by assuming complete incoherence, corresponding to $\lambda_\rho = 1$. Here we use the method of Sjöstrand [49], which simulates the enhancement due to the identical-particle effect. Finally, we compute the ratio $b(q)$ of the pion distributions of same-sign pairs with Bose symmetrization

to the one without, as a function of the invariant mass q . In Fig. 14a we show the resulting enhancement $b_{L_c}(q)$ for our two previously-used values of L_c , confronted with the corresponding distribution obtained by the OPAL collaboration [43] at $Q = 91$ GeV. It is remarkable how well this comparison with the experimental data allows us to separate the two choices of L_c in our calculations. Clearly the value $L_c = 0.8$ fm appears to be strongly favored. In fact, the average source size in this case turns out $\sigma_\rho = 0.84$ fm, which is almost identical to the average cluster size determined from Figs. 10 and 11. On the other hand, this value is well in the range of the pion source radius determined by OPAL, $\sigma_\rho^{exp} = 0.93 \pm 0.17$ fm with $\lambda_\rho^{exp} = 0.87 \pm 0.14$.

We may thus conclude that our presumed identification of $L_c \simeq \sigma_\rho$ indeed has physical relevance that provides a unique relation between the parameter L_c and the experimentally-observed pion emission source radius. With this important insight, it would be interesting to investigate this issue in more detail, because it provides a promising method to extract properties of the partons' space-time evolution and cluster formation from the measured particle distributions. Since the structure of the perturbative parton cascade development is projected locally onto the cluster distribution, which itself maps on the hadron spectra, the characteristic shape of the Bose enhancement $b(q)$ will depend only on the local environment, which may in turn depend on the physical situation (vacuum, as considered here, or medium, as, e.g., in deep-inelastic lepton-nucleus scattering or nucleus-nucleus collisions). Thus, by comparing, for instance, the Bose-Einstein correlations measured in $e^+e^- \rightarrow \text{hadrons}$ to high-energy heavy-ion collisions, one might extract specific features of perturbative QCD in a finite-density and -temperature medium, which are absent in vacuum [24, 50].

As an illustrative example of such a comparison, we show in Fig. 14b the ratio $b_{0.6\text{ fm}}(q)/b_{0.8\text{ fm}}(q)$ of the curves in Fig. 14a. Although the individual curves in Fig. 14a are very similar to each other, their ratio is a very sensitive quantity that filters out clearly their subtle difference. It is evident that a smaller L_c gives rise to a significantly stronger enhancement at low masses $k \lesssim 300$ MeV, peaked at about 1.5 times the pion mass. Fig. 14b also shows that the results for $Q = 34$ GeV and $Q = 91$ GeV are identical, even for this sensitive ratio, which implies that the specifics of the Bose-Einstein effect and Bose enhancement are independent of the energy, in agreement with what is observed

experimentally [44].

6. SUMMARY AND PERSPECTIVES

In conclusion, we have presented a novel approach to the dynamics of parton-hadron conversion and confinement, based on an effective QCD field theory and a kinetic multi-particle description in real time and complete phase space. Our formulation provides an extension of the well-understood perturbative QCD parton evolution to account for the full space-time history traced from parton cascade development, via cluster formation and decay, all the way to the production of final hadrons. The essential points in our approach may be summarized as follows.

- (i) We have constructed a scale-dependent Lagrangian that incorporates *both* parton and hadron degrees of freedom. It is manifestly gauge- and Lorentz-invariant, and consistent with the scale and chiral symmetry properties of QCD. The introduction of the scale $L(r)$ determines locally which are the relevant degrees of freedom around a given space-time point r .
- (ii) The formulation recovers QCD with its symmetry properties at short space-time distances, and merges into an effective low-energy description of hadronic degrees of freedom at large distances. In between the two regimes it interpolates as determined by the scale- (L -)changing dynamics, and results in a transformation from partonic to hadronic degrees of freedom.
- (iii) The dynamics is described by a set of coupled kinetic equations that derive from the field equations of motion, and yield a real-time description in both position and momentum space, constrained by the uncertainty principle.

As a test application, we have considered the prototype reaction $e^+e^- \rightarrow \text{hadrons}$ where the fragmentation of parton jets and their hadronization serves as a generic process that can also be imagined as an integral part of more complex reactions. We investigated in detail the specifics of the time evolution of parton shower, cluster formation and hadron production in phase space, which extends the usual QCD evolution techniques that are limited to momentum space and integrated over time. The consistency with experimental data was tested, and we found good agreement with measured hadron spectra. A prospective method

to extract the characteristics of the space-time development from Bose-Einstein correlations of identical hadrons was suggested. Our main results are:

(i) The details of the parton-hadron conversion are controlled by the quantity L_c , the spatial separation of neighbouring color charges in their restframe, which defines the scale at which non-perturbative confinement forces become substantial. The value of L_c is determined by the choice of the bag constant B and the condensate value χ_0 . All other macroscopic quantities which characterize the evolution, such as pressure, energy density, the time scale of the transition, etc., are then determined self-consistently. The found values are in agreement with common phenomenology.

(ii) The time scale obtained for the transition is a remarkable result: the local conversion of partons to clusters occurs very rapidly ($\approx 0.1 - 0.2 \text{ fm}$), but the global time scale for the transition of the system as a whole is long ($\approx 10 - 30 \text{ fm}$).

(iii) The QCD features of the perturbative parton evolution are projected unscathed onto cluster and hadron distributions, because the conversion is a local, universal mechanism. As a consequence the multiplicities of charged hadrons and their momentum spectra are predetermined by the preceding parton evolution, which we find in good agreement with experiments.

(iv) Our main result is the sensitivity of the Bose-Einstein correlations among identical pions due to Bose symmetry. It allows us to identify the parameter L_c with the hadron emission source radius measured in experiments, and to fix its value rather precisely to $L_c \simeq 0.8 \text{ fm}$. Moreover, the ratio of Bose enhancement of same-sign pions in different scenarios or physical situations can provide a very sensitive probe of the environment in which the parton system evolves. It can be exploited to study, e.g., modifications to parton evolution in finite-density media.

It is interesting to note that our model appears to be able to correlate successfully such diverse quantities as the macroscopic bag constant B , the microscopic length scale L_c for the parton-hadron transition, the associated critical temperature T_c , and the magnitude of measured Bose-Einstein correlations.

Finally we comment on future applications. These are manifold, as the advocated picture of parton-hadron conversion is universally applicable to any dynamical process

where the issue of hadronization arises. Since the strength of our statistical real-time description lies in resolving the details of the space-time structure, situations where parton cascades undergo interactions with an environment would be the interesting to investigate. Let us give three examples:

a) In *deep-inelastic lepton-nucleus scattering* the primary quark struck by the photon can travel and reinteract before hadronizing, and produce a cascade of secondary partons that differs from a parton shower in vacuum. The secondaries are themselves potential candidates for hard re-interactions, and can lead to a specific A (atomic number) dependence for the final-state hadron production. Clearly, here it is essential to keep track of the parton-hadron conversion at each point in time and space, because partons that reinteract will not be able to hadronize before they approach the free-streaming regime.

b) In *high-energy nucleus-nucleus collisions* [51] ($\sqrt{s}/A \gtrsim 200$ GeV) the parton density of the highly Lorentz-contracted nuclei is very large already in the initial state, and is further increased by the materialization and multiplication of partons [24]. Therefore multiple scatterings of partons can easily lead to a large number of simultaneously-evolving cascades that also can interact with each other. In order to resolve such an intertwined structure of parton interactions, the space-time dynamics of the system *must* be taken into account. Again, here a microscopic space-time description of parton-hadron conversion is crucial to resolve the details of such an intertwined structure of parton interactions and the following hadron formation process, depending on the local densities of surrounding parton and hadron matter.

c) The *QCD phase transition* from a hot, deconfined quark-gluon plasma to excited hadron matter as occurred in the early Universe [37] is of long-standing theoretical interest. Lattice QCD calculations to date can only investigate the critical behaviour in the vicinity of the transition temperature. Moreover, a dynamical evolution of the system deviating significantly from thermal equilibrium is not achievable. In view of the future experimental programs at RHIC and LHC, it will soon become possible to recreate the QCD phase transition in the laboratory [52], and to investigate its dynamics in the real world. It is clear that the conversion of a quark-gluon plasma into hadrons is a much more complicated process than the hadronization of final-state partons in free space (as in e^+e^- annihilation), or dilute systems (as in hadron-hadron collisions). In heavy-ion collisions the transition is

expected to proceed as a complex evolution of expansion and cooling of the plasma, perhaps through a mixed parton-hadron phase, until a purely hadronic phase is reached [53]. Therefore, a fully dynamical and microscopic hadronization scheme as proposed in this paper is needed to trace the space-time-dependent cooling and expansion process from the parton to the hadron phase.

References

- [1] P. Hasenfratz and J. Kuti, Phys. Rep. **40**, 75 (1998); R. Goldflam and L. Wilets, Phys. Rev. **D25**, 1951 (1982); H. B. Nielsen and A. Patkos, Nucl. Phys. **B195**, 137 (1982).
- [2] See e.g.: A. H. Mueller (ed.), *Perturbative Quantum Chromodynamics*, Advanced Series on Directions in High Energy Physics, Vol. 5 (World Scientific, Singapore 1989).
- [3] J. Gasser and H. Leutwyler, Phys. Rep. **87**, 77 (1982); E. Witten, Nucl. Phys. **B223**, 422, 433 (1983); J. Gasser and H. Leutwyler, Nucl. Phys. **B250**, 465 (1985); U. Vogl and W. Weise, Prog. Part. Nucl. Phys. **27**, 195 (1991).
- [4] M. A. Shifman, A. I. Vainshtein, and V. A. Zakharov, Nucl. Phys. **B147**, 448 (1979).
- [5] B. Webber, Ann. Rev. Nucl. Part. Sci. **36**, 253 (1986); preprint Cavendish-HEP-943/17.
- [6] F. Karsch, Nucl. Phys. (Proc. Suppl.) **B9**, 357 (1989).
- [7] J. Ellis and K. Geiger, preprint CERN-TH. 95-34.
- [8] K. Geiger, Phys. Rev. **D51**, 2345 (1995).
- [9] R. Friedberg and T. D. Lee, Phys. Rev. **D15**, 1694 (1977); **D16**, 1096 (1977); T. D. Lee, *Particle Physics and Introduction to Field Theory* (Harwood Academic Press, New York, 1981).
- [10] G. Fai, J. Perry and L. Wilets, Phys. Lett. **B208**, 1 (1988).
- [11] G. Krein, P. Tang, L. Wilets and A.G. Williams, Nucl. Phys. **A523**, 548 (1991).
- [12] J. Schechter, Phys. Rev. **D21**, 3393 (1981).

- [13] J. Ellis and J. Lanik, Phys. Lett. **B150**, 289 (1984).
- [14] B. A. Campbell, J. Ellis, and K. A. Olive, Phys. Lett. **B235**, 325 (1990); Nucl. Phys. **B345**, 57 (1990).
- [15] R. Friedberg and T. D. Lee, Phys. Rev. **D18**, 2623 (1978).
- [16] E. Shuryak, *The QCD Vacuum, Hadrons and Superdense Matter* (World Scientific Publ., Singapore, 1987).
- [17] L. Wilets, *Nontopological Solitons* (World Scientific, Singapore 1989), and references therein.
- [18] J. Kapusta, Nucl. Phys. **148**, 461 (1979), 461; E. V. Shuryak, Phys. Rep. **115**, 151 (1984); N. P. Landsman and C. G. van Weert, Phys. Rep. **145**, 141 (1987).
- [19] K. Geiger, in preparation.
- [20] L. P. Kadanoff and G. Baym, *Quantum Statistical Mechanics* (Benjamin Publ., New York 1962).
- [21] K. Chou, Z.Su, B. Hao, and L. Yu, Phys. Rep. **118**, 1 (1985).
- [22] F. J. Dyson, Phys. Rev. **75**, 1736 (1949); J. Schwinger, Phys. Rev. **75**, 651 (1949).
- [23] M. Hillery, R. F. O'Connell, M. O. Scully and E. Wigner, Phys. Rep. **106**, 121 (1984).
- [24] K. Geiger, Phys. Rep. in press; CERN-TH 7313/94 (1994).
- [25] S. de Groot, W. A. van Leuwen and C. G. van Weert, *Relativistic Kinetic Theory*, North Holland, Amsterdam 1980.
- [26] S. Coleman, Nucl. Phys. **262**, 263 (1985).
- [27] D. Amati and G. Veneziano, Phys. Lett. **B83**, 87 (1979); G. Marchesini, L. Trentadue and G. Veneziano, Nucl. Phys. **B181**, 335 (1981).
- [28] See e.g.: A. L. Fetter and J. D. Walecka, *Quantum Theory of Many-Particle Systems* (McGraw-Hill, New York, 1971).
- [29] Yu. L. Dokshitzer, D. I. Dyakonov, and S. I. Troyan, Phys. Rep. **58**, 269 (1980).

- [30] A. Bassetto, G. Nardelli and R. Soldati, *Yang-Mills theories in algebraic non-covariant gauges* (World Scientific, Singapore 1991).
- [31] A. Bassetto, M. Ciafaloni, and G. Marchesini, Phys. Rep. **100**, 201 (1983).
- [32] Yu. L. Dokshitzer, V. A. Khoze, A. H. Mueller, and S. I. Troyan, Advanced Series on Directions in High Energy Physics, Vol. 5 (Editions Frontieres, Gif-sur-Yvette Cedex, France, 1991)
- [33] K. Konishi, A. Ukawa, and G. Veneziano, Nucl. Phys. **B157**, 45 (1979).
- [34] K. Geiger, Phys. Rev. **D46**, 4965 (1992).
- [35] D. Amati, A. Bassetto, M. Ciafaloni, G. Marchesini, and G. Veneziano, Nucl. Phys. **B173**, 429 (1980).
- [36] J. S. Langer, Ann. Phys. **54**, 258 (1969); L. Csernai and J. I. Kapusta, Phys. Rev. **D46**, 1379 (1992).
- [37] J. Ellis, in the *Proceedings of the Les Houches Summer School on Cosmology and Large Scale Structure*, Les Houches, 1993.
- [38] K. Geiger, Phys. Rev. **D47**, 133 (1993).
- [39] B. R. Webber, Nucl. Phys. **B238**, 492 (1984).
- [40] R. Hagedorn, *Thermodynamics of Strong Interactions*, Cargèse Lectures in Physics, Vol. 6 (1973).
- [41] J. Ignatius, K. Kajantie, H. Kurki-Suonio, and M. Laine, Phys. Rev. **D50**, 3738 (1994).
- [42] D. Thomas, D. N. Schramm, K. A. Olive, G. J. Mathews, B. S. Meyer, and B. D. Fields, Astrophys. J. **406**, 569 (1993); *ibid.* **430**, 291 (1994).
- [43] TPC Collaboration, Phys. Rev. **D31**, 996 (1985); TASSO Collaboration, Z. Phys. **C30**, 355 (1986); MARK II Collaboration, Phys. Rev. **D39**, 39 (1989); OPAL Collaboration, Phys. Lett. **B267**, 143 (1991); ALEPH Collaboration, Z. Phys. **C54**, 75 (1992); DELPHI Collaboration, Phys. Lett. **B268**, 201 (1992).

- [44] S. Haywood, Rutherford-Appleton preprint RAL-94-074, and references therein.
- [45] S. L. Wu, Phys. Rep. **107**, 59 (1984); B. Naroska, Phys. Rep. **148**, 67 (1987).
- [46] T. Hebbeker, Phys. Rep. **217**, 69 (1992); S. Bethke and J. E. Pilcher, Ann. Rev. Nucl. Part. Sci. **42**, 251 (1992).
- [47] M. Althoff *et al.*, Z. Phys. **C14**, 5 (1983).
- [48] M. G. Bowler, Z. Phys. **C29**, 617 (1985).
- [49] T. Sjöstrand, CERN-TH.7112/93.
- [50] K. Geiger, Phys. Rev. **D49**, 3234 (1994).
- [51] *Quark Matter '93*, Proceedings of the Tenth International Conference on Ultra-relativistic Nucleus-Nucleus Collisions, Borlänge, Sweden, 1993, edited by H. A. Gustafsson *et al.* [Nucl. Phys. **A566**, 1c (1994)].
- [52] B. Müller, in the proceedings of the *Workshop on Pre-equilibrium Parton Dynamics in Heavy Ion Collisions*, edited by X. N. Wang, LBL-34831 / CONF-9308181; and in Rep. Prog. Phys. (in press).
- [53] L. Csernai, J. I. Kapusta, G. Kluge, and E.E. Zabrodin, Z. Phys. **C58**, 453 (1993); L. Csernai, in the proceedings of *Strangeness '95*, Tucson, 1995.

TABLE CAPTIONS

Table 1: Obtained values for phenomenological quantities involved in our description. The bag constant B and the condensate value $\chi_0 = \langle 0|\chi|0\rangle$ are fixed inputs. The values of the length scales L_c , L_χ , the global conversion time scale $\tau_0 \propto L_0$, and the magnitude of the surface tension σ_c , are then extracted from the numerical simulation. Also listed is the associated critical temperature T_c , the mass scale of the lightest scalar glueball m_χ , and the estimate for the gluon condensate G_0 .

Table 2: $e^+e^- \rightarrow \text{hadrons}$ at $Q = 34$ GeV: Average multiplicities of partons $\langle n_{qg} \rangle = \langle n_g \rangle + \sum_f \langle n_q + n_{\bar{q}} \rangle$, of clusters $\langle n_{cl} \rangle$, and of charged hadrons $\langle n_{ch} \rangle$, plus the contribution of pions, kaons and protons, in comparison with measured particle multiplicities [47].

FIGURE CAPTIONS

Figure 1: Schematic behaviour of $\kappa_L(\chi)$, eq. (16) and $\mu(\chi)$, eq. (17).

Figure 2: Form of the scale-dependent potential $\mathcal{V}(L)$, eq. (21), where L_χ characterizes the point of inflection at χ_χ , L_c marks the point when the two minima are degenerate at χ_c , and L_0 when the potential has a single absolute minimum at χ_0 . The value at $\chi = 0$ is equal to the vacuum pressure (bag constant) B .

Figure 3: Diagrammatic representation of **a)** the two-point Green functions $S, D, \Delta, \tilde{\Delta}$; **b)** the self energies $\Sigma, \Pi, \Xi, \tilde{\Xi}$; **c)** the corresponding Dyson-Schwinger equations (30). *Notation:* Fat (thin) lines indicate fully-dressed (bare) propagators, shaded circles and boxes denote the full quark and gluon vertex functions, black circles and boxes with attached loops represent the local interactions with the collective fields χ and U via the potential \mathcal{V} , eq. (21).

Figure 4: Illustration of the simultaneous evolution in space-time r and – ‘orthogonal’ to it – in energy-momentum p of the Wigner functions $F_\alpha(r, p)$, according to the transport and constraint equations (34) and (35). The self-consistent solution of these equations corresponds to summing over all possible quantum paths r , accounting for fluctuations in p , under the constraint of the uncertainty principle.

Figure 5: Schematics of the different stages of the process $e^+e^- \rightarrow \text{hadrons}$. The initial $q\bar{q}$ pair with large invariant mass Q initiates a shower which can be followed perturbatively until $L \simeq L_\chi$. At this point the conversion into clusters sets in, which is completed around $L = L_0$ and followed by the decay of clusters into hadron states.

Figure 6: Diagrammatic representation of the kinetic equations (49). **a)** The operator \hat{K} describes free propagation plus the effect of the mean field. **b)** The integral operators $\hat{A}, \hat{B}, \hat{C}, \dots$ include the squared amplitudes for the various interaction processes among the different particle species, which change of the particle distributions according to the balance of gain (+) and loss (−) terms.

Figure 7: **a)** Space-time evolution of the parton density profile (in arbitrary units) in the (r_z, r_\perp) -plane at different times in the center-of-mass frame of the initial dijet system with energy $Q = 100$ GeV. **b)** Corresponding development of the cluster density profile as it builds up in time due to the conversion of partons.

Figure 8: **a)** Time evolution of the kinetic pressures P_{qg} of partons and P_χ of pre-hadronic clusters for $q\bar{q}$ -initiated jet evolution, for total jet energies $Q = 10$ GeV (top) and $Q = 100$ GeV (bottom). The dashed and full lines correspond to the two parameter choices $(B^{1/4}, \chi_0) = (240, 200)$ MeV and $(B^{1/4}, \chi_0) = (180, 100)$ MeV, resulting in $L_c = 0.6$ fm and $L_c = 0.8$ fm, respectively. **b)** As a), but for a gg -initiated jet evolution.

Figure 9: Total transverse momentum $p_\perp(t)$, eq. (88), generated during the time evolution of the system in the center-of-mass of the initial dijet system, in correspondence to Fig. 8: **a)** case of $q\bar{q}$ -initiated jet evolution (top); **b)** case of a gg -initiated jet evolution (bottom).

Figure 10: Cluster spectra for $L_c = 0.6$ fm (top), and $L_c = 0.8$ fm (bottom), and total jet energies $Q = 10$ (100) GeV. **a)** Distribution of the cluster sizes of clusters formed from neighboring partons. **b)** Associated cluster mass spectrum.

Figure 11: As Fig. 10, but now with the additional constraint of a maximum allowed invariant mass per cluster of $M_{crit} = 4$ GeV: **a)** cluster size distribution; **b)** cluster mass spectrum.

Figure 12: **a)** Total gluon and quark multiplicities $\langle n_{qg} \rangle = \langle n_g \rangle + \sum_f \langle n_q + n_{\bar{q}} \rangle$, for $L_c = 0.6$ (0.8) fm as a function of energy Q . **b)** The corresponding ratios of charged hadrons to partons $\langle n_{ch} \rangle / \langle n_{qg} \rangle$, and of clusters to partons, $\langle n_{cl} \rangle / \langle n_{qg} \rangle$.

Figure 13: **a)** Calculated average charged multiplicity versus total energy Q in e^+e^- annihilation events, in comparison with experimental data [45]. **b)** Momentum spectra of charged hadrons with respect to the variable $\ln(1/x)$, where $x = 2E/Q$, at $Q = 34$ GeV and $Q = 91$ GeV, confronted with distributions measured at PEP/PETRA and LEP [46].

Figure 14: **a)** Simulated Bose-Einstein enhancement $b_{L_c}(q)$ as a function of the pair mass q of same-sign pion pairs for the two values of L_c at total energy $Q = 91$ GeV. The data points are from the OPAL experiment [43] at LEP. **b)** Ratios of the enhancements $b_{0.6 fm}(q)/b_{0.8 fm}(q)$ for total jet energies $Q = 34$ GeV and $Q = 91$ GeV.

	$B^{1/4} = 230 \text{ MeV}$ $\chi_0 = 200 \text{ MeV}$	$B^{1/4} = 180 \text{ MeV}$ $\chi_0 = 100 \text{ MeV}$
$L_c \text{ (fm)}$	0.6	0.8
$L_\chi \text{ (fm)}$	0.45	0.65
$\tau_0 \text{ (fm)}$	8.5 (21)	10 (26)
$\sigma_c^{1/3} \text{ (MeV)}$	40	48
$T_c \text{ (MeV)}$	160	125
$m_\chi \text{ (GeV)}$	1.05	1.30
$G_0 \text{ (GeV/fm}^3\text{)}$	1.25	0.50

Table 1

$Q = 34 \text{ GeV}$	$L_c = 0.6 \text{ fm}$	$L_c = 0.8 \text{ fm}$	Experiment Ref. [47]
$\langle n_{gg} \rangle$	9.7	8.6	—
$\langle n_{cl} \rangle$	8.7	7.7	—
$\langle n_{ch} \rangle$	14.1	13.5	13.6 ± 0.9
$\langle n_{\pi^+} + n_{\pi^-} \rangle$	11.4	10.9	10.3 ± 0.4
$\langle n_{K^+} + n_{K^-} \rangle$	1.6	1.5	2.0 ± 0.2
$\langle n_p + n_{\bar{p}} \rangle$	0.8	0.7	0.8 ± 0.1

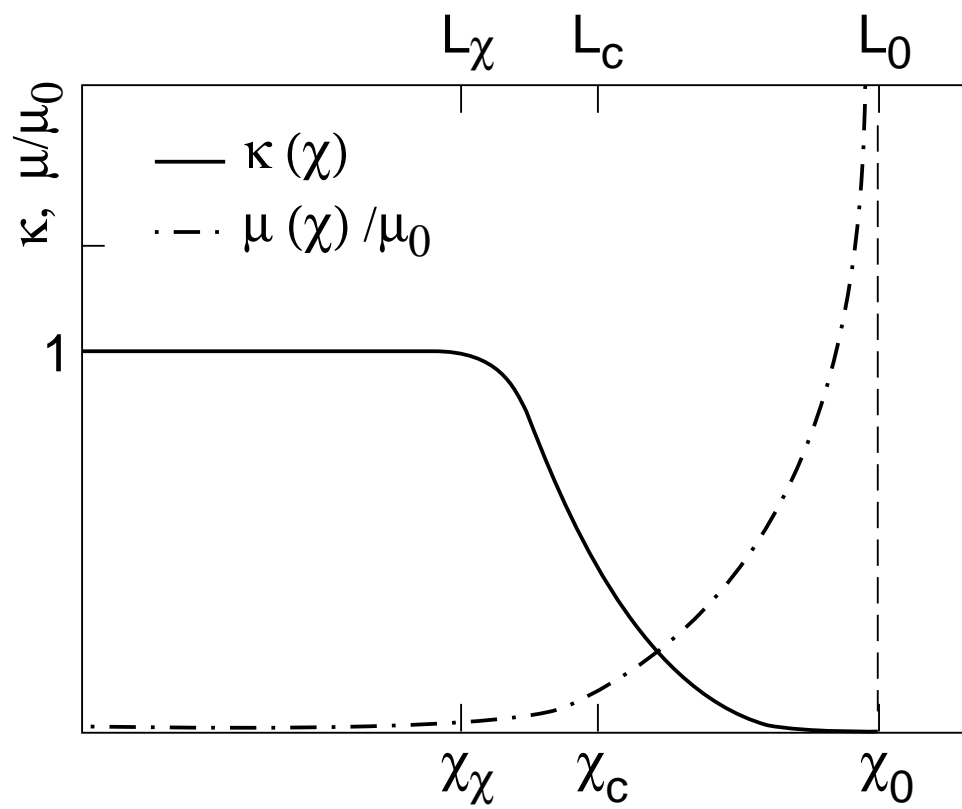
Table 2

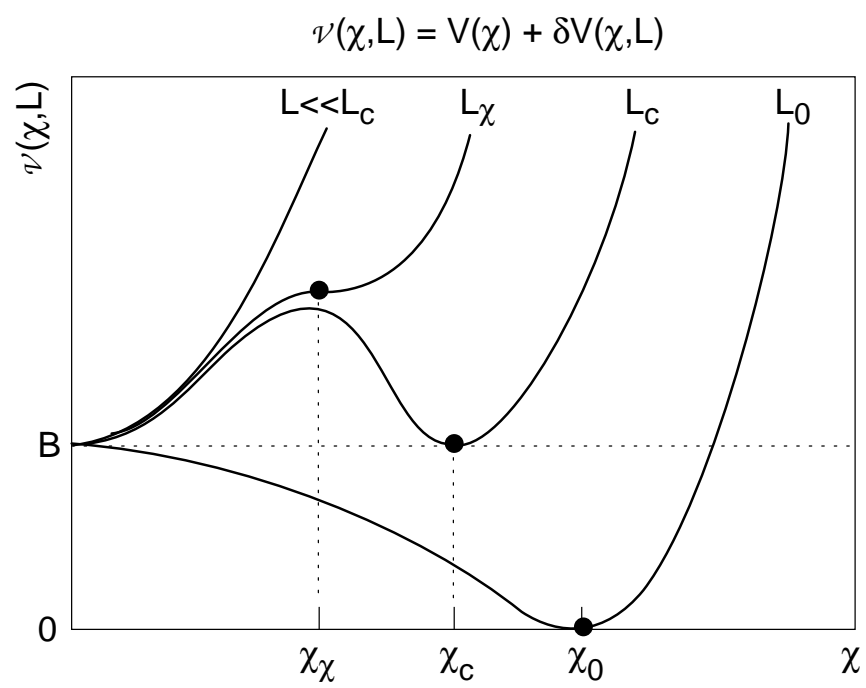
This figure "fig1-1.png" is available in "png" format from:

<http://arXiv.org/ps/hep-ph/9503349v1>

This figure "fig2-1.png" is available in "png" format from:

<http://arXiv.org/ps/hep-ph/9503349v1>





Propagators:



Self-energies :

$$(i) \quad \Sigma = \Sigma_{qg} + \Sigma_{q\chi}$$

$$\Sigma_{qg} = \text{Diagram: A fermion line with a gluon loop. The vertex is labeled } \Gamma_{qg}.$$

$$\Sigma_{q\chi} = \text{Diagram: A fermion line with a scalar loop. The vertex is labeled } \Gamma_{q\chi}.$$

$$(ii) \quad \Pi = \Pi_{gq} + \Pi_{gg} + \Pi_{g\chi}$$

$$\Pi_{gq} = \text{Diagram: A gluon line with a fermion loop. The vertex is labeled } \Gamma_{gq}.$$

$$\Pi_{gg} = \text{Diagram: A gluon line with a gluon loop. The vertex is labeled } \Gamma_{gg}.$$

$$\Pi_{g\chi} = \text{Diagram: A gluon line with a scalar loop. The vertex is labeled } \Gamma_{g\chi}.$$

$$(iii) \quad \Xi = \Xi_{\chi\chi} + \Xi_{\chi U} + \Xi_{\chi q} + \Xi_{\chi g}$$

$$\Xi_{\chi\chi} = \text{Diagram: A fermion line with a fermion loop. The vertex is labeled } \Gamma_{\chi\chi}.$$

$$\Xi_{\chi U} = \text{Diagram: A fermion line with a scalar loop. The vertex is labeled } \Gamma_{\chi U}.$$

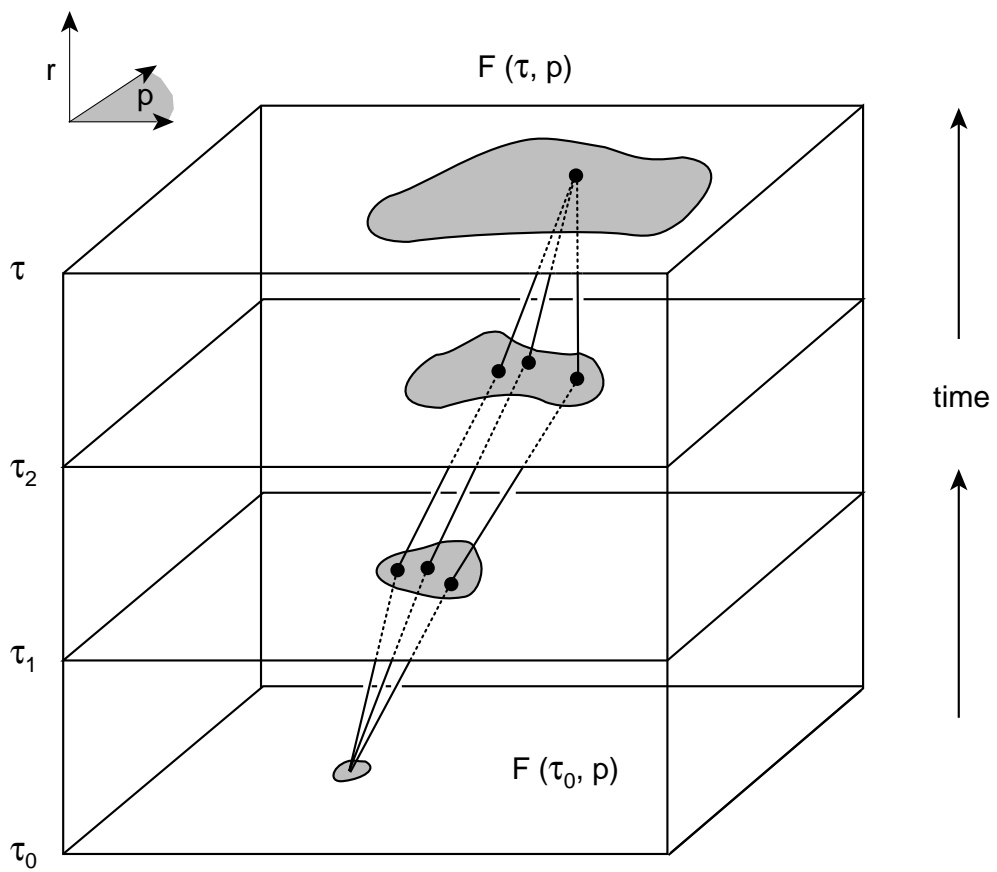
$$\Xi_{\chi q} = \text{Diagram: A fermion line with a fermion loop. The vertex is labeled } \Gamma_{\chi q}.$$

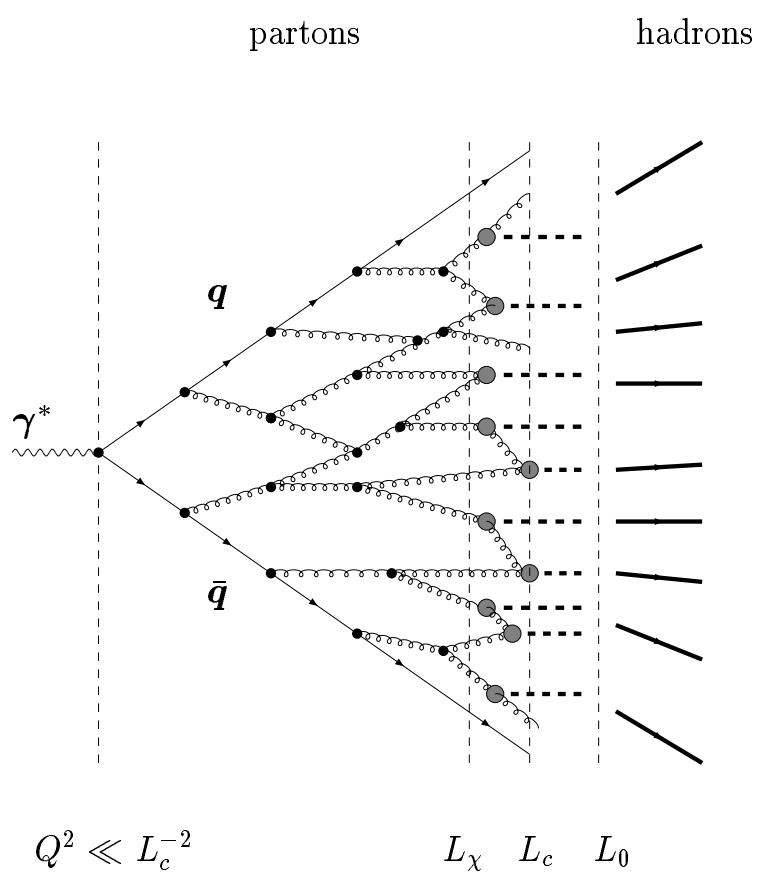
$$\Xi_{\chi g} = \text{Diagram: A gluon line with a gluon loop. The vertex is labeled } \Gamma_{\chi g}.$$

$$(iv) \quad \tilde{\Xi} = \Xi_{U\chi} = \Xi_{\chi U}$$

Dyson-Schwinger equations:

$$\begin{aligned}
 \text{(i)} \quad S &= S_0 + \Sigma S = \text{diagram} + \Gamma_{qg} \text{diagram} + \Gamma_{q\chi} \text{diagram} \\
 \text{(ii)} \quad D &= D_0 + \Pi D = \text{diagram} + \Gamma_{gq} \text{diagram} + \Gamma_{gg} \text{diagram} \\
 \text{(iii)} \quad \Delta &= \Delta_0 + \Xi \Delta = \text{diagram} + \Gamma_{\chi\chi} \text{diagram} + \Gamma_{\chi U} \text{diagram} + \Gamma_{\chi q} \text{diagram} + \Gamma_{\chi g} \text{diagram} \\
 \text{(iv)} \quad \tilde{\Delta} &= \tilde{\Delta}_0 + \tilde{\Xi} \tilde{\Delta} = \text{diagram} + \Gamma_{U\chi} \text{diagram}
 \end{aligned}$$





(i)
$$\begin{array}{c} p \\ \xrightarrow{\hat{\mathcal{K}}_q} \end{array} \equiv \begin{array}{c} p \\ \longrightarrow \end{array} + \begin{array}{c} p \\ \xrightarrow{\mathbf{x}} \\ \mu(\chi) \end{array}$$

(ii)
$$\begin{array}{c} p \\ \xrightarrow{\hat{\mathcal{K}}_g} \end{array} \equiv \begin{array}{c} p \\ \xrightarrow{\quad} \end{array} + \begin{array}{c} p \\ \xrightarrow{\mathbf{x}} \\ (\kappa(\chi)-1)^{-1} \end{array}$$

(iii)
$$\begin{array}{c} p \\ \xrightarrow{\hat{\mathcal{K}}_\chi} \end{array} \equiv \begin{array}{c} p \\ \xrightarrow{\quad} \end{array} + \begin{array}{c} p \\ \xrightarrow{\mathbf{x}} \\ m_\chi = \left(\frac{\partial^2 V}{\partial \chi^2} \right)^{1/2} \end{array}$$

(iv)
$$\begin{array}{c} p \\ \xrightarrow{\hat{\mathcal{K}}_U} \end{array} \equiv \begin{array}{c} p \\ \xrightarrow{\quad} \end{array} + \begin{array}{c} p \\ \xrightarrow{\mathbf{x}} \\ m_U = \left(\frac{\partial^2 V}{\partial U^2} \right)^{1/2} \end{array}$$

$$(i) \left[\text{diagram} - \text{diagram} \right] + \text{diagram} - \left[\text{diagram} - \text{diagram} \right] - \text{diagram}$$

\hat{A}_q^{qg}
 $\hat{A}_g^{q\bar{q}}$
 $\hat{B}_{qg}^{q\chi}$
 $\hat{B}_{q\bar{q}}^{\chi\chi}$

$$(ii) \left[\text{diagram} - \text{diagram} \right] - \text{diagram} + \left[\text{diagram} + \text{diagram} \right]$$

\hat{A}_g^{gg}
 $\hat{A}_q^{q\bar{q}}$
 $\hat{A}_q^{g\bar{q}}$
 $\hat{B}_{gg}^{\chi\chi}$
 $\hat{B}_{gq}^{\chi q}$

$$(iii) \text{diagram} + \left[\text{diagram} + \text{diagram} \right] + \text{diagram}$$

$\hat{C}_{gg}^{\chi\chi}$
 $\hat{C}_{gq}^{\chi q}$
 $\hat{C}_{q\bar{q}}^{\chi\chi}$

$$- \text{diagram} - \left[\text{diagram} + \text{diagram} \right]$$

\hat{D}_χ^U
 \hat{E}_χ^h

$$(iv) \text{diagram} - \left[\text{diagram} + \text{diagram} \right]$$

\hat{D}_χ^U
 \hat{E}_U^h

This figure "fig1-2.png" is available in "png" format from:

<http://arXiv.org/ps/hep-ph/9503349v1>

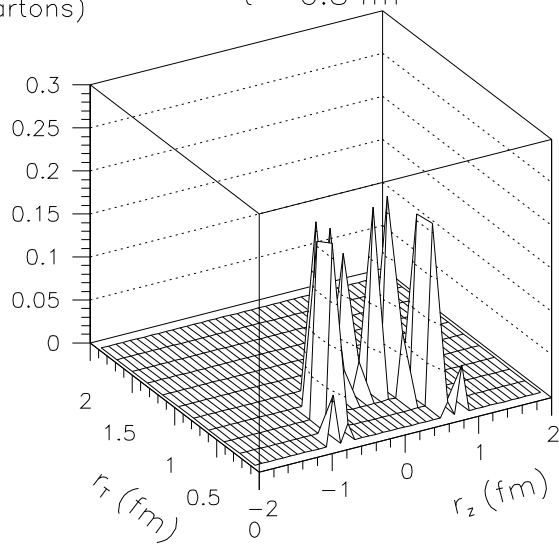
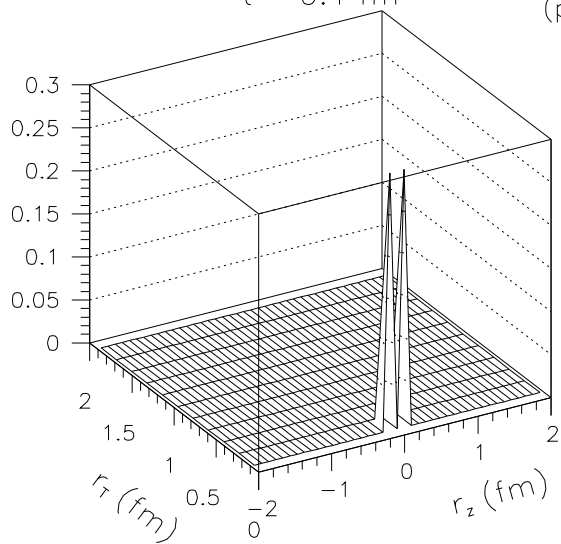
This figure "fig2-2.png" is available in "png" format from:

<http://arXiv.org/ps/hep-ph/9503349v1>

particle density
(partons)

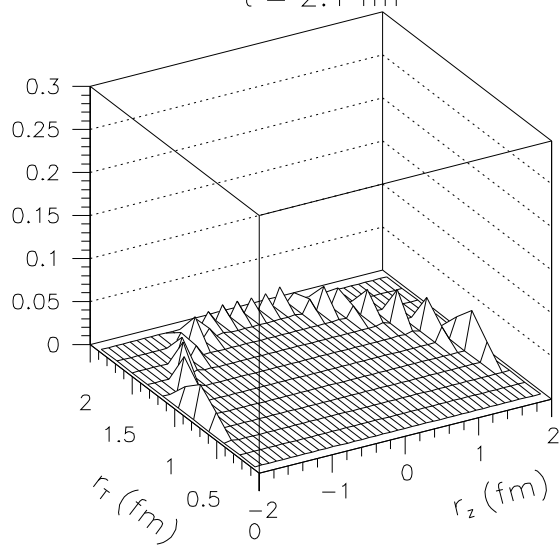
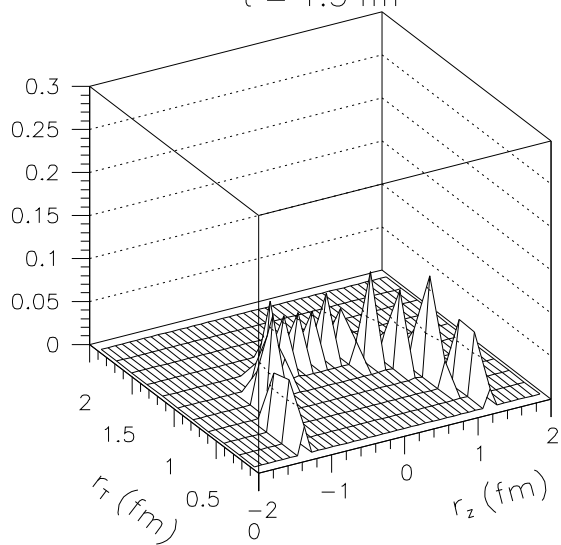
$t = 0.1 \text{ fm}$

$t = 0.8 \text{ fm}$



$t = 1.3 \text{ fm}$

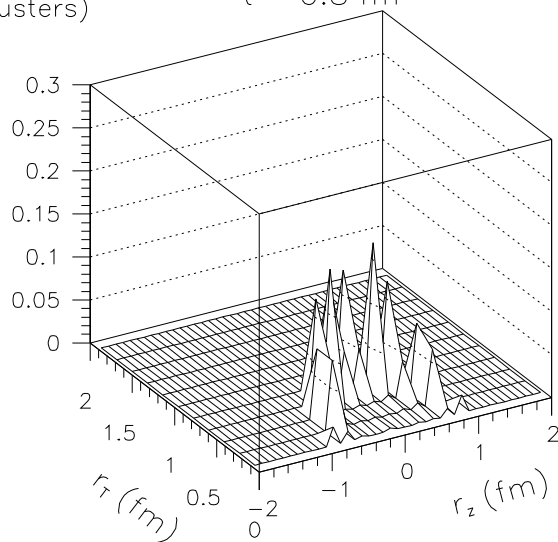
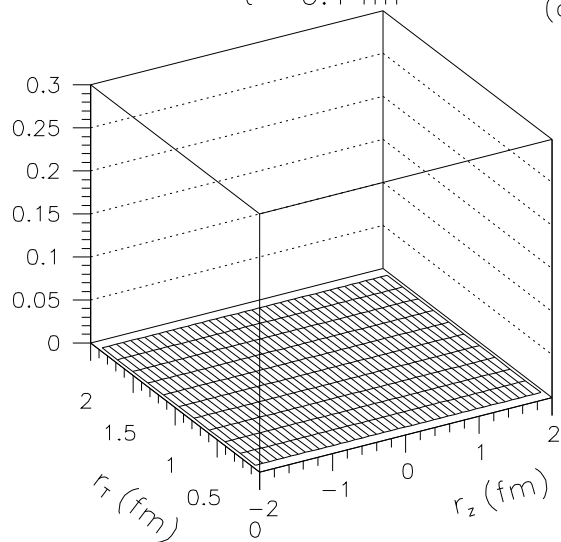
$t = 2.1 \text{ fm}$



particle density
(clusters)

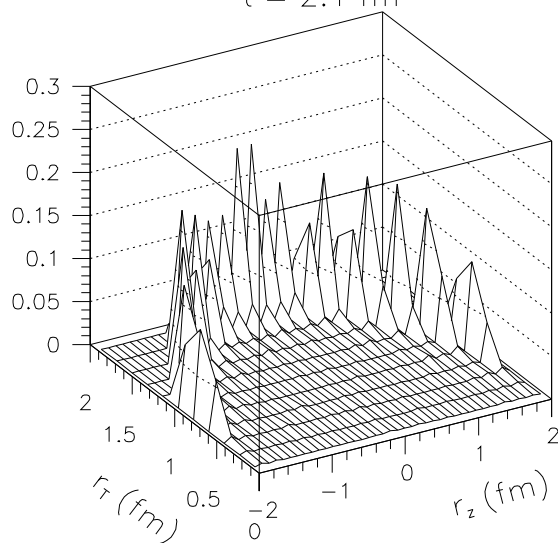
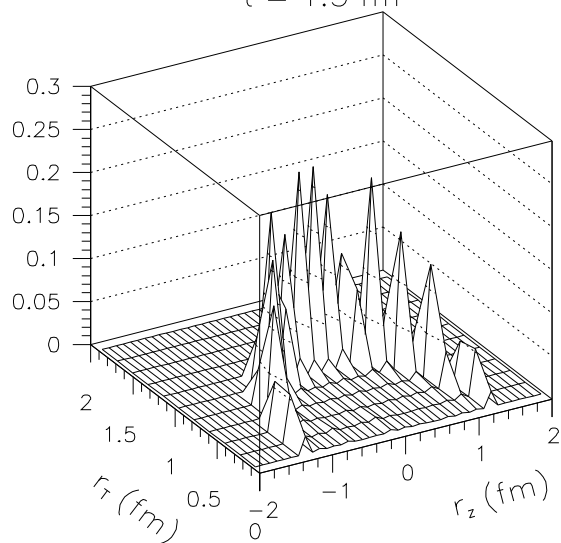
$t = 0.1 \text{ fm}$

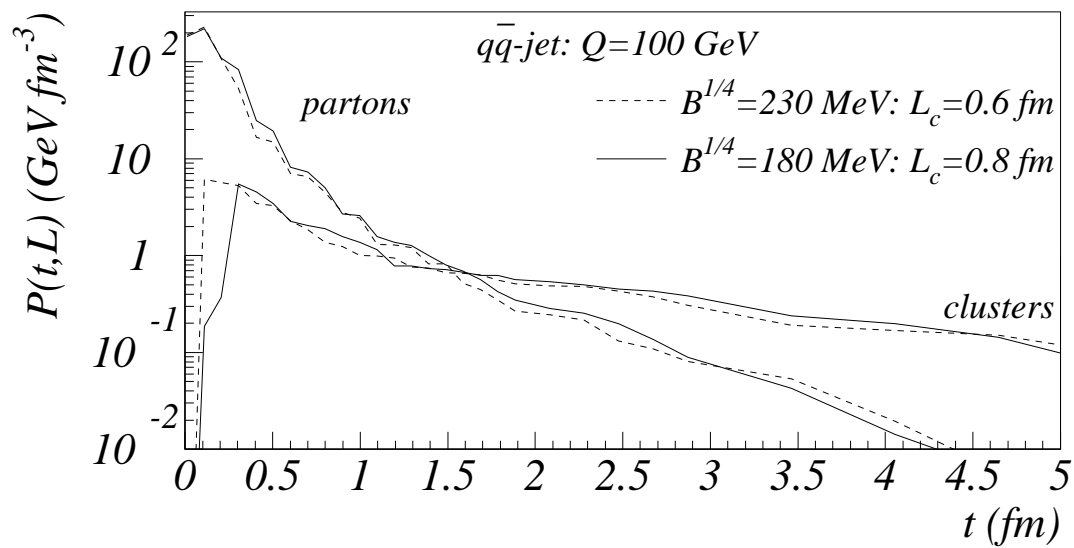
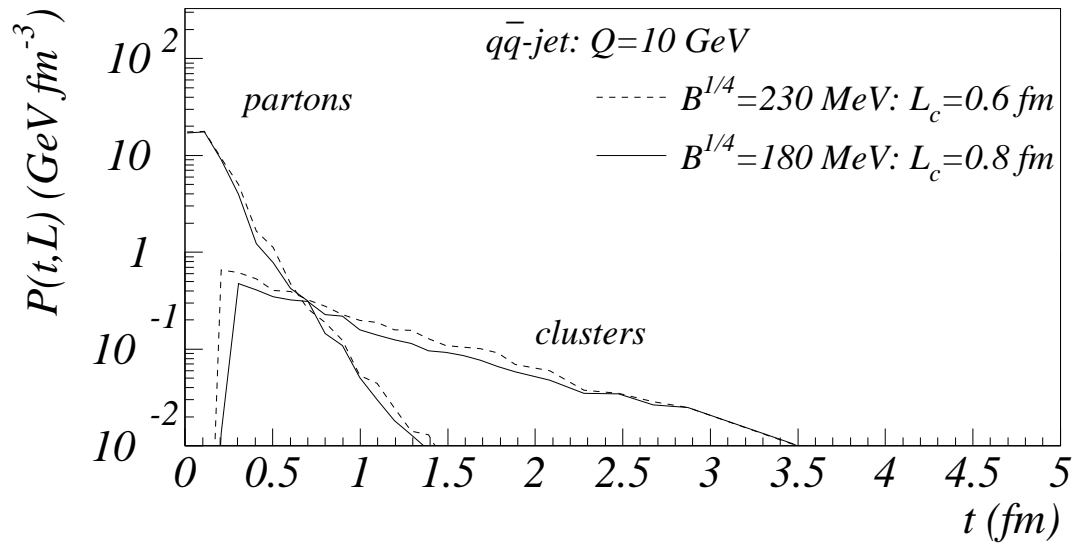
$t = 0.8 \text{ fm}$

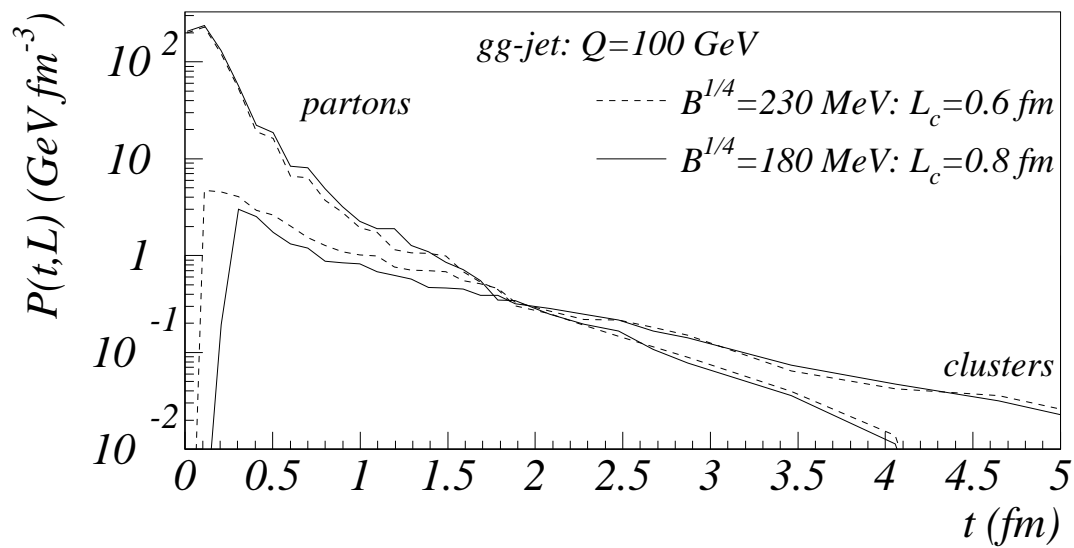
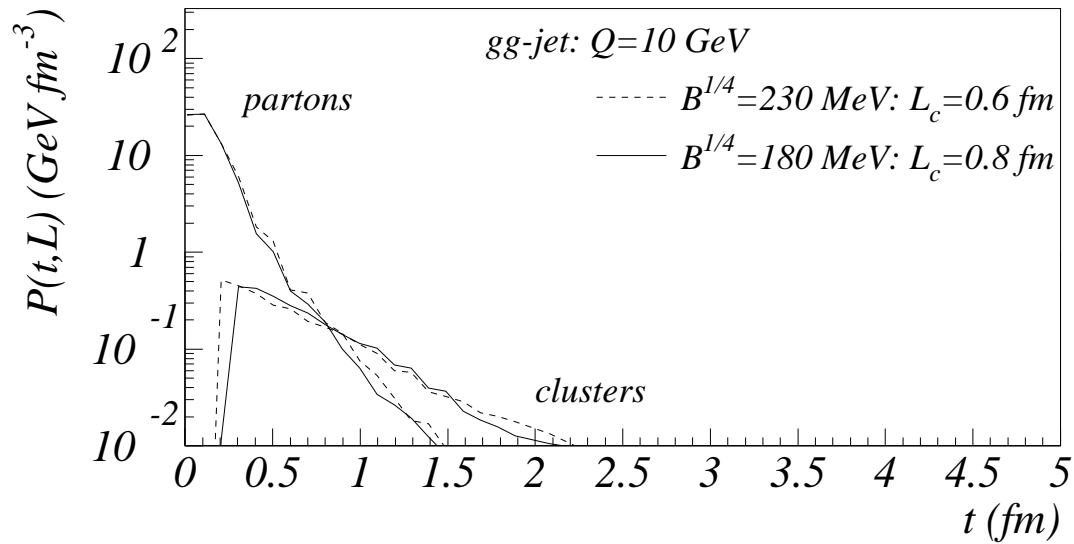


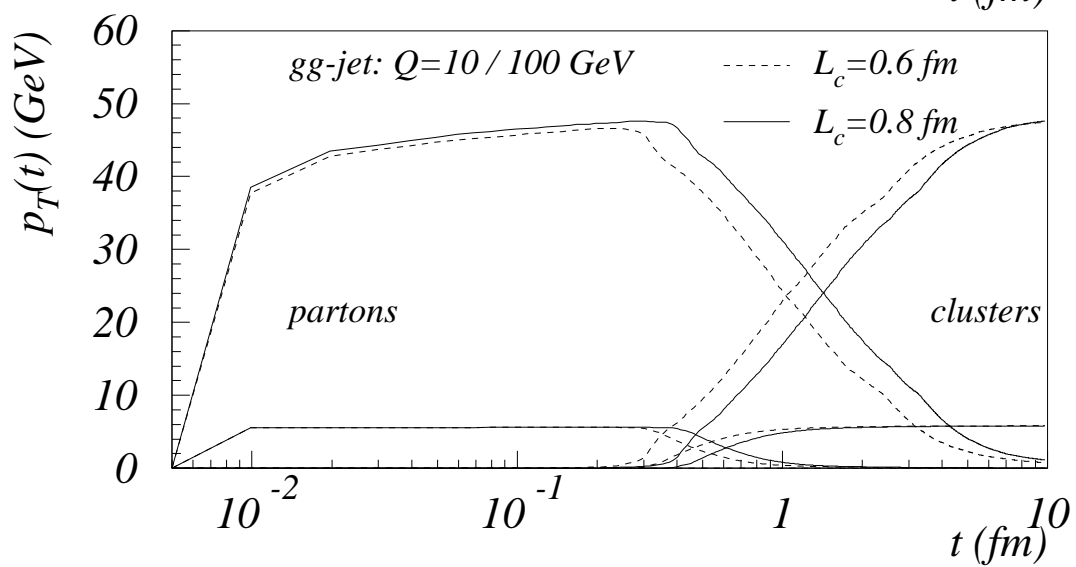
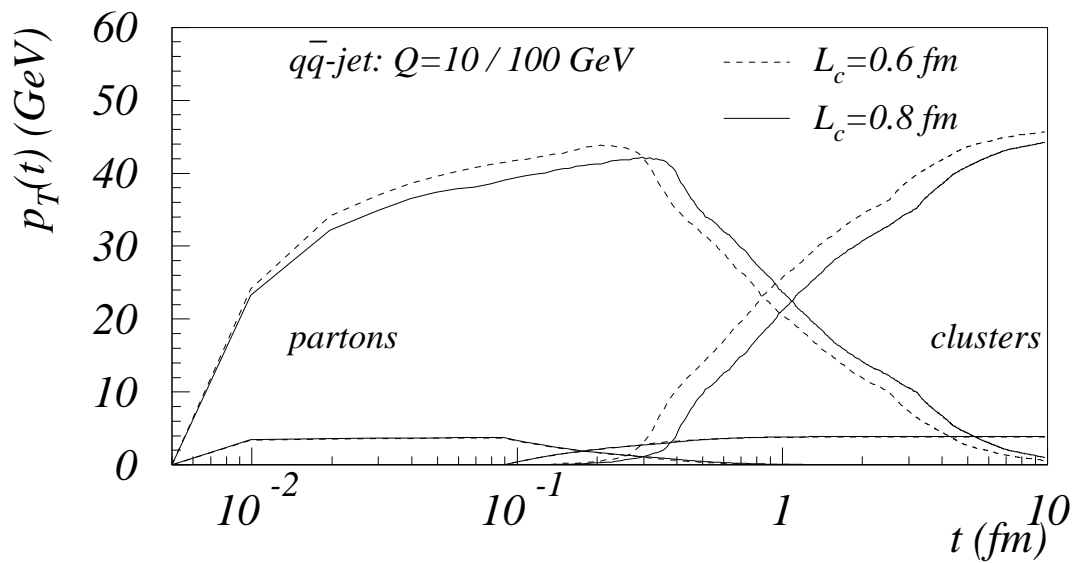
$t = 1.3 \text{ fm}$

$t = 2.1 \text{ fm}$

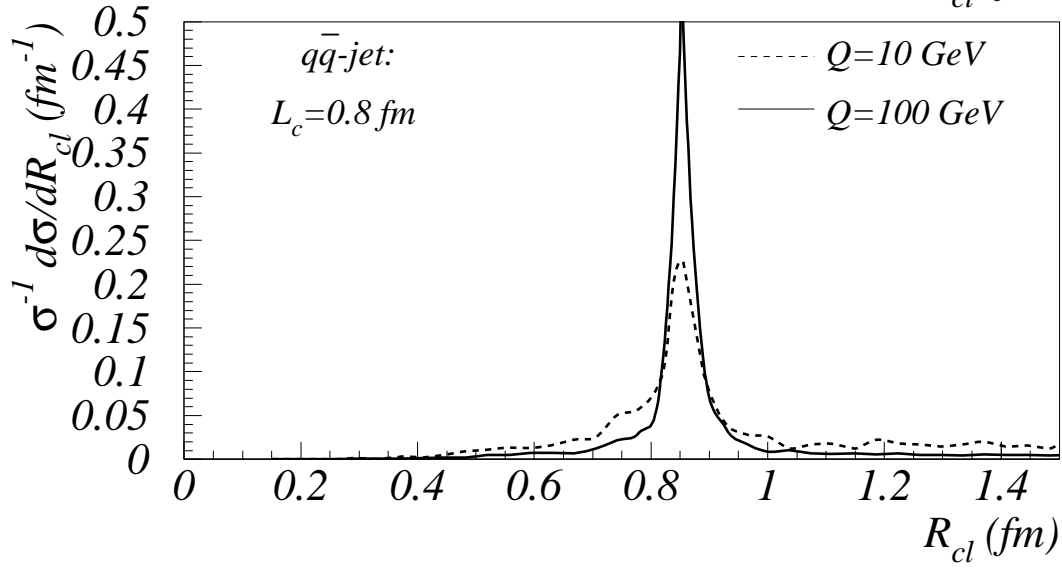
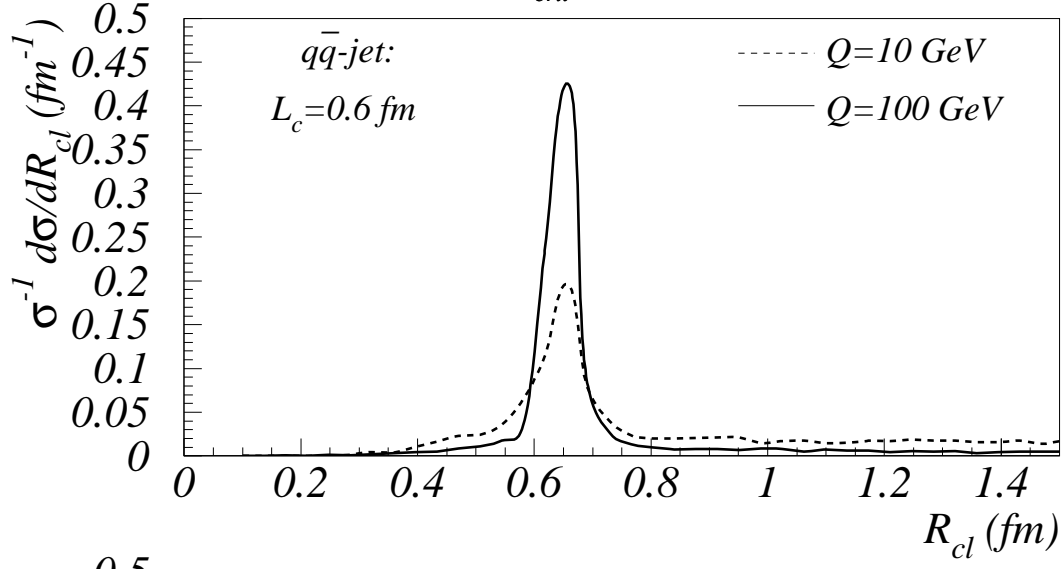


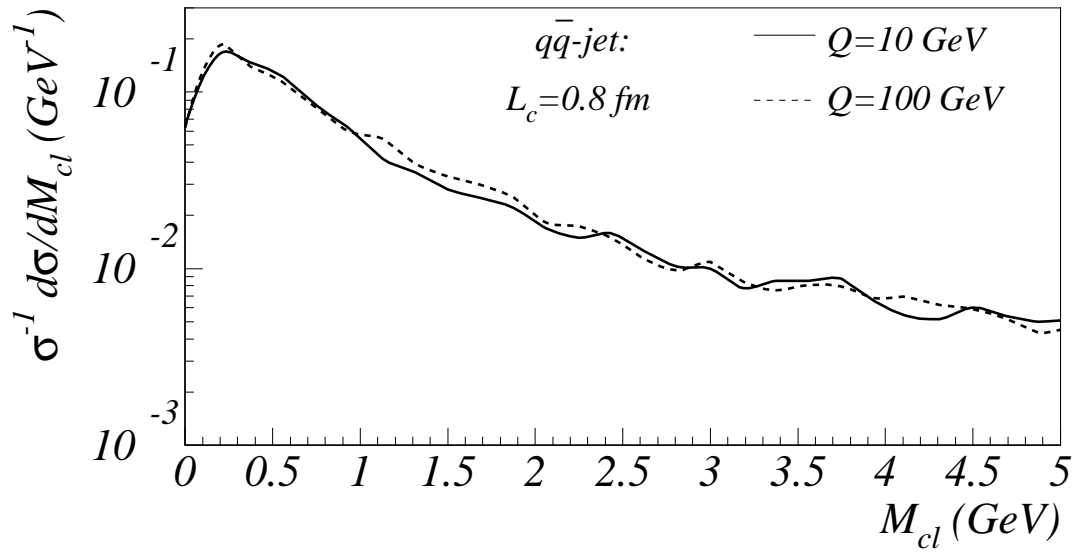
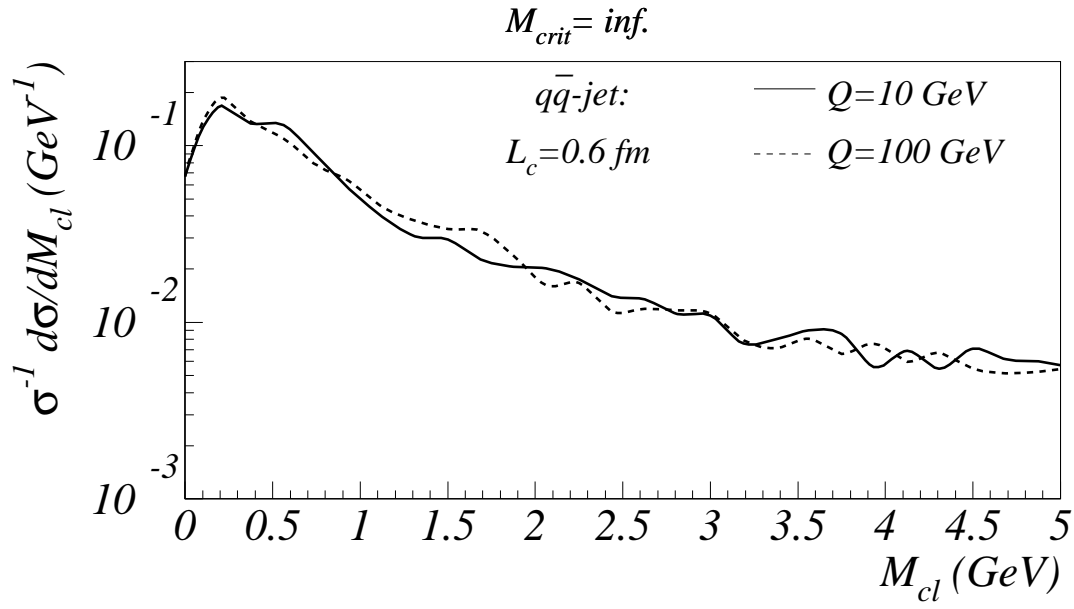




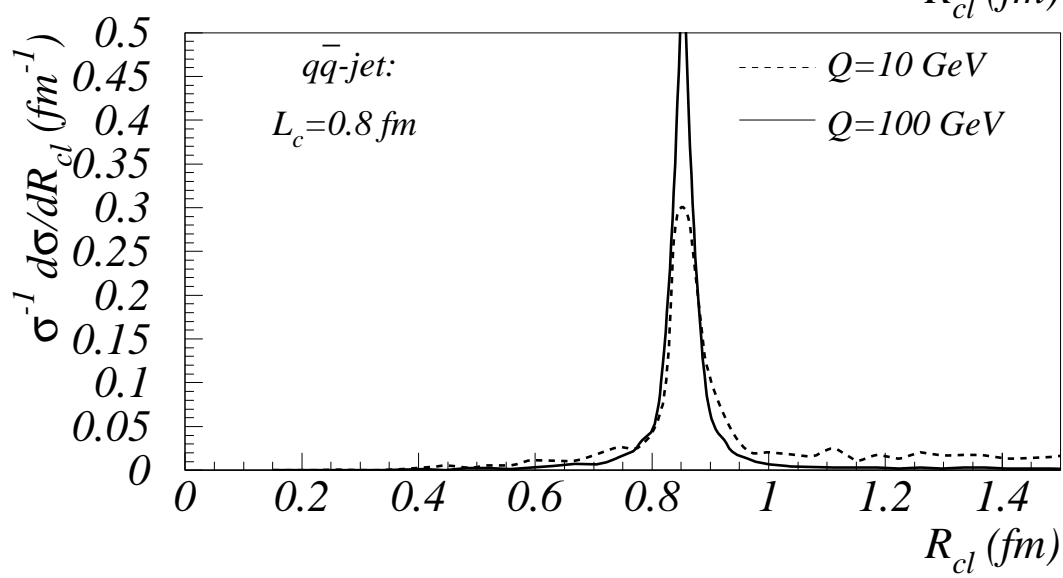
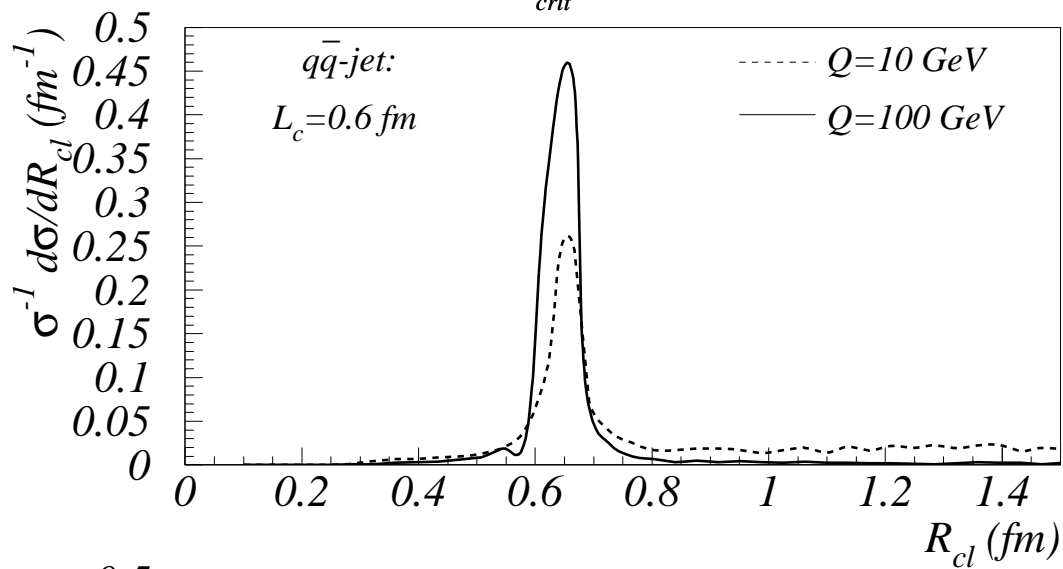


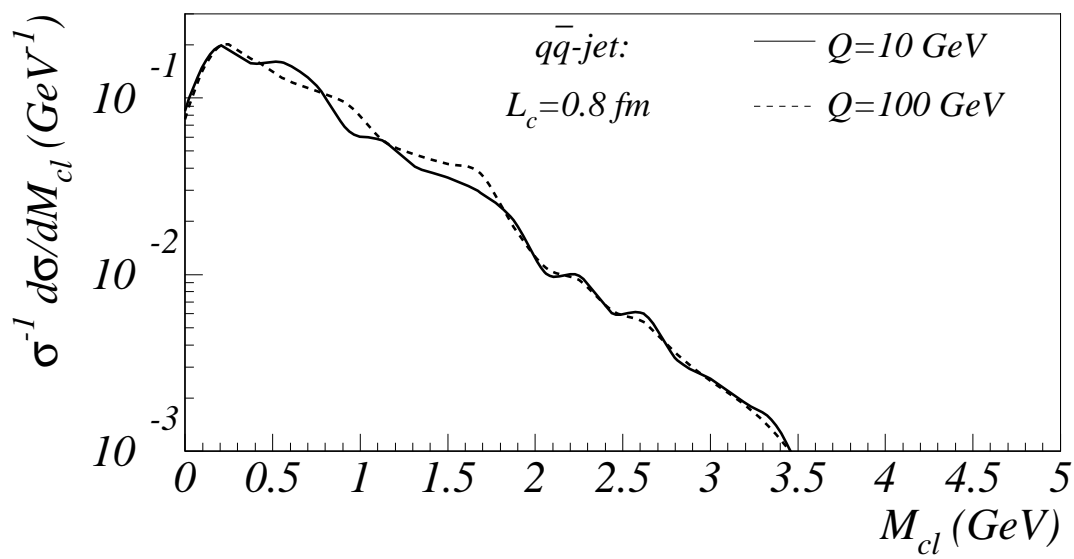
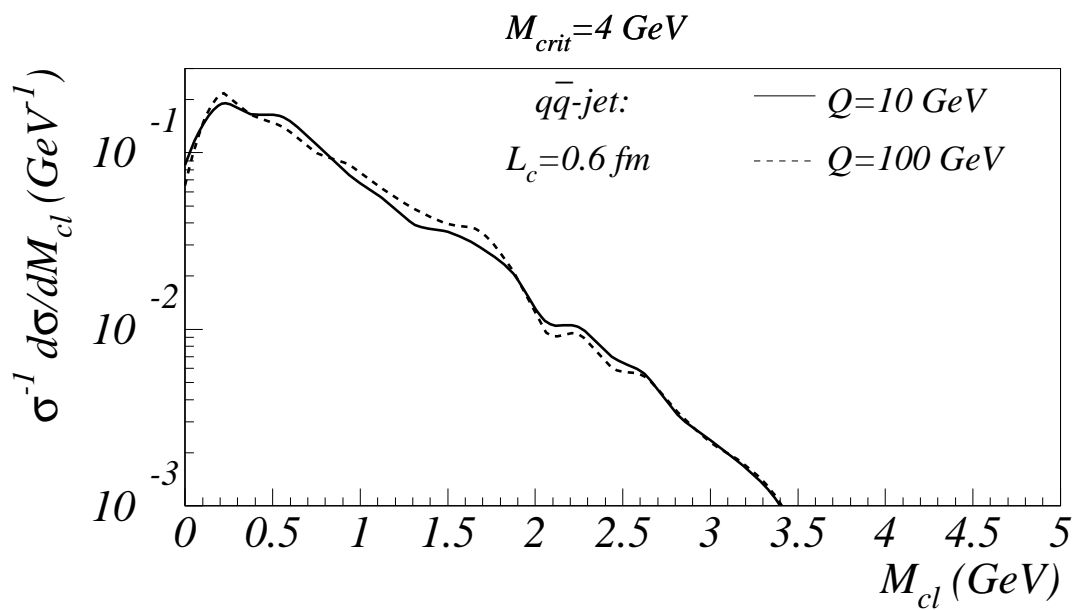
$M_{crit} = inf.$

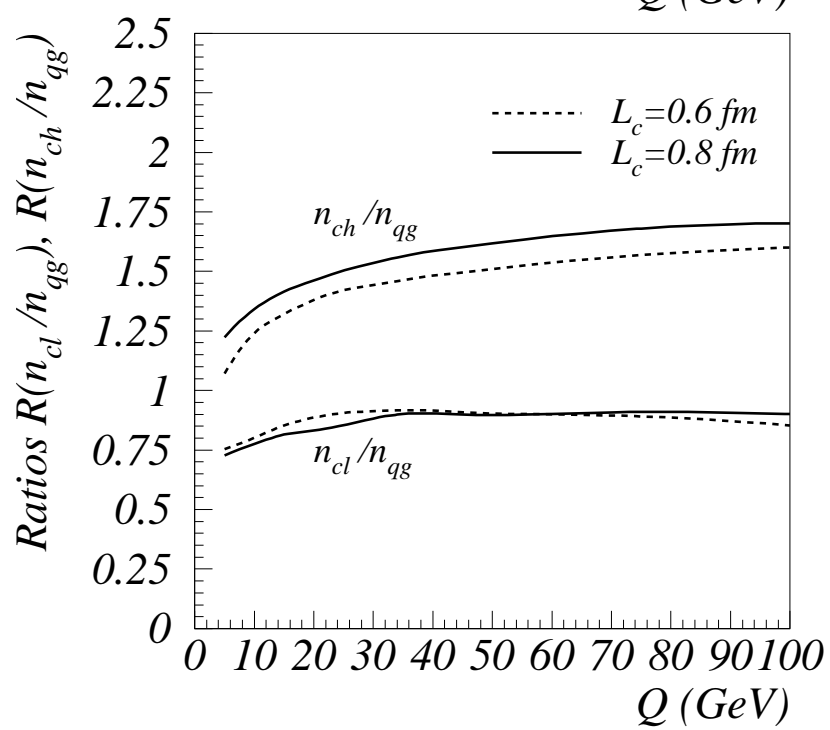
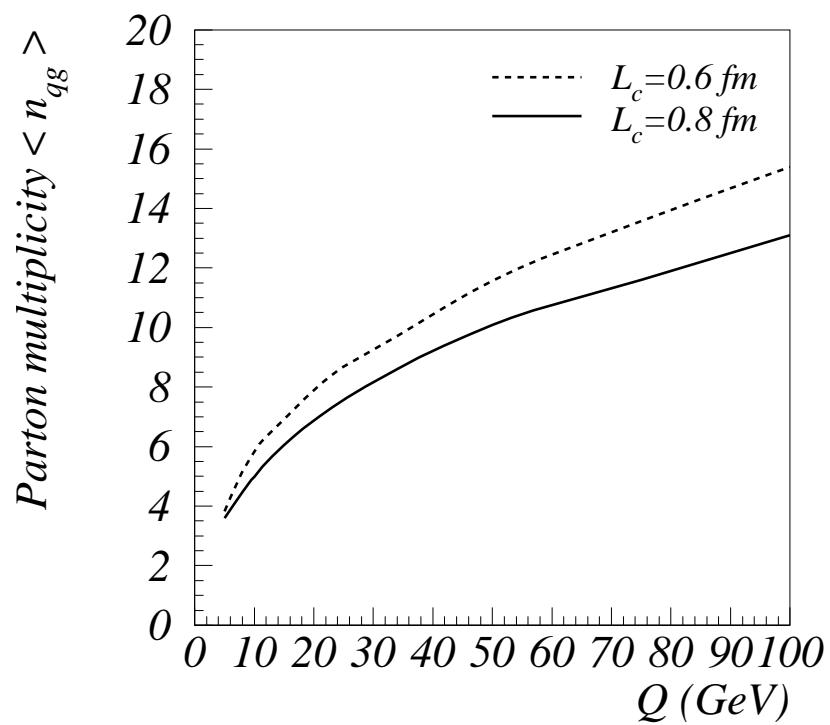


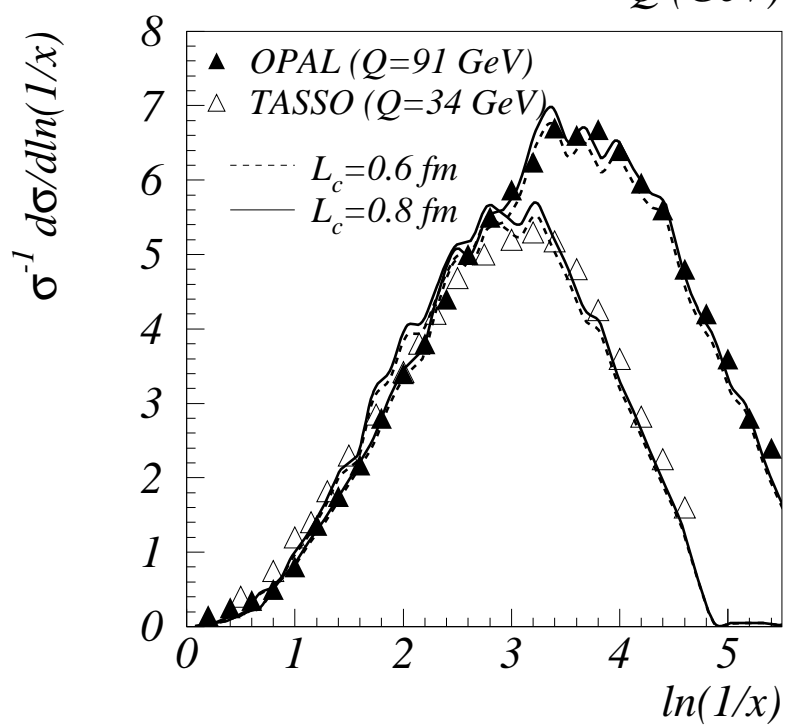
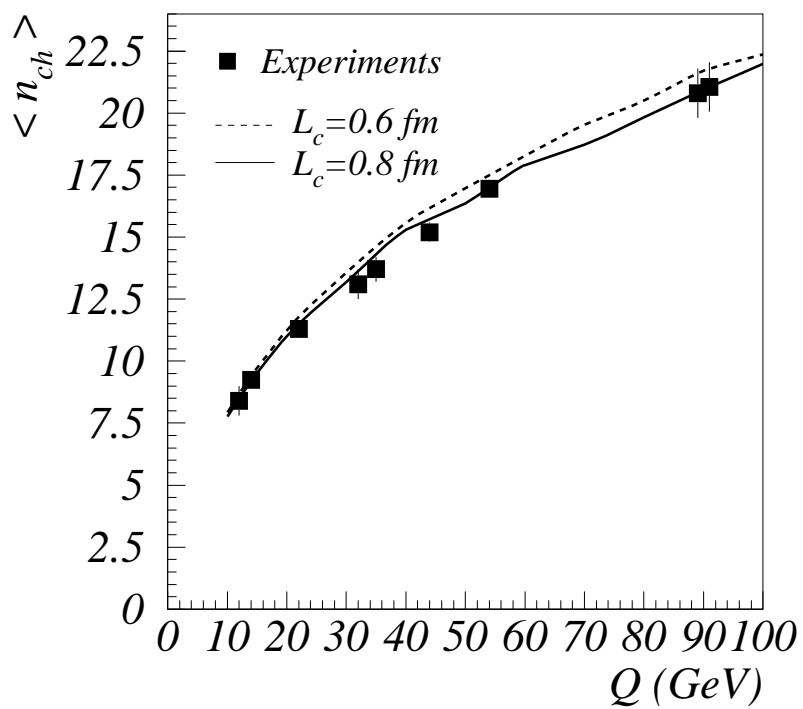


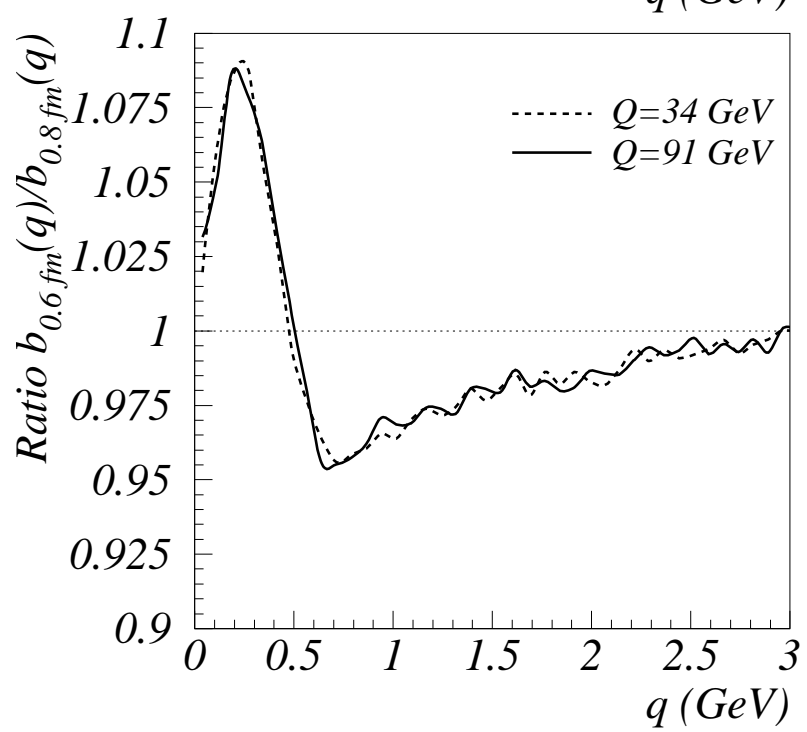
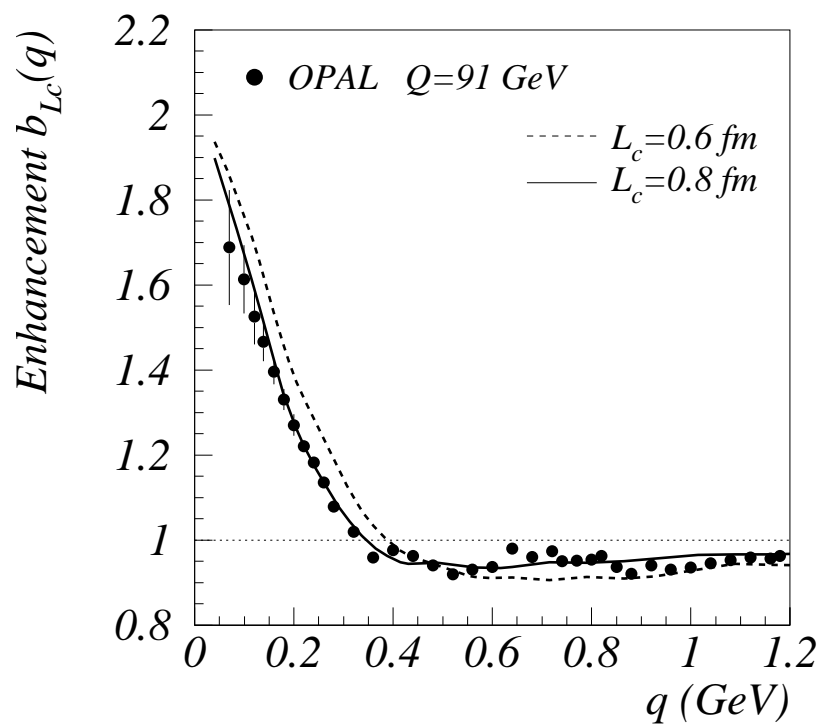
$M_{\text{crit}}=4 \text{ GeV}$











This figure "fig1-3.png" is available in "png" format from:

<http://arXiv.org/ps/hep-ph/9503349v1>

This figure "fig2-3.png" is available in "png" format from:

<http://arXiv.org/ps/hep-ph/9503349v1>

This figure "fig1-4.png" is available in "png" format from:

<http://arXiv.org/ps/hep-ph/9503349v1>

This figure "fig2-4.png" is available in "png" format from:

<http://arXiv.org/ps/hep-ph/9503349v1>

This figure "fig1-5.png" is available in "png" format from:

<http://arXiv.org/ps/hep-ph/9503349v1>

This figure "fig2-5.png" is available in "png" format from:

<http://arXiv.org/ps/hep-ph/9503349v1>

This figure "fig1-6.png" is available in "png" format from:

<http://arXiv.org/ps/hep-ph/9503349v1>

This figure "fig2-6.png" is available in "png" format from:

<http://arXiv.org/ps/hep-ph/9503349v1>

This figure "fig1-7.png" is available in "png" format from:

<http://arXiv.org/ps/hep-ph/9503349v1>

This figure "fig2-7.png" is available in "png" format from:

<http://arXiv.org/ps/hep-ph/9503349v1>

This figure "fig1-8.png" is available in "png" format from:

<http://arXiv.org/ps/hep-ph/9503349v1>

This figure "fig2-8.png" is available in "png" format from:

<http://arXiv.org/ps/hep-ph/9503349v1>

This figure "fig1-9.png" is available in "png" format from:

<http://arXiv.org/ps/hep-ph/9503349v1>

This figure "fig2-9.png" is available in "png" format from:

<http://arXiv.org/ps/hep-ph/9503349v1>

This figure "fig2-10.png" is available in "png" format from:

<http://arXiv.org/ps/hep-ph/9503349v1>

This figure "fig2-11.png" is available in "png" format from:

<http://arXiv.org/ps/hep-ph/9503349v1>

This figure "fig2-12.png" is available in "png" format from:

<http://arXiv.org/ps/hep-ph/9503349v1>